

A novel alloy design approach in developing CoNi-based high entropy superalloy using high entropy alloys thermodynamic and spark plasma

Downloaded from: https://research.chalmers.se, 2026-08-12 18:36 UTC

Citation for the original published paper (version of record):

Mohammadzdeh, A., De Nardi, A., Omidbakhsh, F. et al (2024). A novel alloy design approach in developing CoNi-based high entropy superalloy using high
entropy alloys thermodynamic and spark plasma sintering. Materials Science & Engineering A: Structural Materials: Properties, Microstructure and Processing, 909.
http://dx.doi.org/10.1016/j.msea.2024.146841

N.B. When citing this work, cite the original published paper.

research.chalmers.se offers the possibility of retrieving research publications produced at Chalmers University of Technology. It covers all kind of research output: articles, dissertations, conference papers, reports etc. since 2004. research.chalmers.se is administrated and maintained by Chalmers Library

(article starts on next page)

Materials Science & Engineering A 909 (2024) 146841

Contents lists available at ScienceDirect

Materials Science & Engineering A

journal homepage: www.elsevier.com/locate/msea

A novel alloy design approach in developing CoNi-based high entropy superalloy using high entropy alloys thermodynamic and spark plasma sintering

Ahad Mohammadzdeh [a,b,*], Alessandro De Nardi [b,c], Faraz Omidbakhsh [d], Dariusz Garbiec [e], Ahmed Fardan [f], Eduard Hryha [f], Amir Mostafaei [g], Jose Manuel Torralba [h,b]

[a] Department of Materials Engineering, Faculty of Engineering, University of Maragheh, Maragheh, P.O. Box 83111-55181, Iran
[b] Imdea Materials Institute, Calle Eric Kandel, 2, 28906, Getafe, Madrid, Spain
[c] Politecnico di Torino, Corso Duca degli Abruzzi, 24, 10129, Torino, Italy
[d] Department of Mechanical Engineering, College of Engineering, Islamic Azad University, Tabriz Branch, Tabriz, Iran
[e] Łukasiewicz Research Network – Poznań Institute of Technology, 6 Ewarysta Estkowskiego St., 61-755, Poznan, Poland
[f] Department of Industrial and Materials Science, Chalmers University of Technology, 412 96, Göteborg, Sweden
[g] Department of Mechanical, Materials, and Aerospace Engineering, Illinois Institute of Technology, 10 W 32nd Street, Chicago, IL, 60616, USA
[h] Universidad Carlos III de Madrid, Av. Universidad 30, 28911, Leganés, Spain

ARTICLE INFO

Keywords:
High entropy superalloys
Spark plasma sintering
Thermodynamical calculations
Powder metallurgy
Microstructure analysis

ABSTRACT

This study introduces an innovative alloy design strategy by integrating HEAs principles to develop CoNi-based high entropy superalloys (HESAs). The powder of designed HESA produced using gas atomization and consolidated using spark plasma sintering (SPS). The alloy design strategy validated by CALPHAD to mitigate detrimental phase precipitation and segregation during powder production, material consolidation, and post-processing heat treatments. CoNi-HESA powder with a calculated mixing entropy of 1.568R was successfully developed and consolidated using SPS. Optimization of SPS parameters at 1175 °C, 10 min, and 100 °C/min achieved a relative density of 99.9 %. Subsequent heat treatments further improved the material's characteristics. Solutionizing at 1190 ± 10 °C for 2 h with water quenching resulted in a fine grain structure of ~7 μm grain size. Aging at 900 °C for 24 h, followed by water quenching, yielded uniformly distributed fine γ′ precipitates comprising approximately 65 % of the γ matrix, without unwanted secondary precipitates or TCP phases. This study demonstrates the effectiveness of the novel approach in designing CoNi-based HESAs and optimizing their properties through careful process parameter selection and post-heat treatment cycles. The combination of thermodynamic calculations, HEA principles, and powder metallurgy techniques offers a promising approach for developing advanced high entropy superalloys with tailored microstructures.

1. Introduction

Co- or CoNi-based superalloys and high entropy alloys (HEAs) are gaining attention as promising alternatives to Ni-based superalloys because of their ability to overcome the current limits of Ni-base superalloys (approaching γ' solvus temperature to Ni melting point) in high-temperature applications. Among the Co-based superalloys, the Co–9Al–9W alloy, which is strengthened by a ternary $Co_3(Al, W)$ intermetallic compound with an ordered $L1_2$ structure, was proposed by Sato et al. [1] and has emerged as a new family of superalloys that can suppress the limitations of matured Ni-based superalloys [2–4]. Co-based superalloys, despite having cuboidal and, in some compositions, high γ' volume fraction after aging, are plagued by critical issues such as a metastable γ' phase, a low γ' solvus temperature ($T_{\gamma'}$), high density (>9 g cm^{-3}), and poor high-temperature oxidation resistance. However, incorporating heavy elements, such as W, in the Co–Al–W alloying system is crucial in precipitating a ternary A_3B phase with an $L1_2$ structure, resulting in a higher density [5–8]. To improve the high-temperature physical and mechanical properties of Co-based superalloys, researchers have explored different strategies, including introducing γ' stabilizers [9–13], such as Ni, Ti, and V, which makes it possible to decrease the number of heavy elements in the alloy [14–18].

* Corresponding author. Imdea Materials Institute, Calle Eric Kandel, 2, 28906, Getafe, Madrid, Spain.
E-mail addresses: amzadeh@ymail.com, amohammadzadeh@maragheh.ac.ir (A. Mohammadzdeh).

https://doi.org/10.1016/j.msea.2024.146841
Received 25 September 2023; Received in revised form 23 April 2024; Accepted 15 June 2024
Available online 17 June 2024
0921-5093/© 2024 The Authors. Published by Elsevier B.V. This is an open access article under the CC BY license (http://creativecommons.org/licenses/by/4.0/).

In 2015, Makineni et al. [3] proposed W-free Co-based superalloys with a density lower than 8.5 g cm^{-3} and a γ' solvus temperature of 866 °C. In another study on W-free Co-based superalloys, Cao et al. [19], using the calculation of phase diagram (CALPHAD) method, developed an eight-component Co-rich high-entropy alloy that demonstrated improved properties compared to the alloy proposed by Makineni et al. [3]. The new alloy had a γ' solvus temperature of 1125 °C and a mass density of 8.28 g cm^{-3}. Additionally, multicomponent Co- or CoNi-based superalloys with more than six alloying elements have been developed to enhance their high-temperature properties, such as adding Cr to improve oxidation resistance [17,19–21].

Recent studies have explored the use of machine learning and CALPHAD methods to design and develop CoNi-based superalloys with a lower density and higher $T_{\gamma'}$. For example, Zhuang et al. [22] developed an eight-element CoNi-based superalloy with a density lower than 8.5 g cm^{-3} and $T_{\gamma'}$ of 1125 °C using a machine learning method. In another study, Zhuang et al. [23] designed and developed a seven-component high-Cr CoNi-based superalloy with a density lower than 8.5 g cm^{-3}, high γ' volume fraction, and $T_{\gamma'}$ of 1090 °C using the CALPHAD method. Currently, the number of elements in Co- or CoNi-based superalloys are increasing in order to improve high temperature properties and they have been developed with up to nine elements [22]. Increasing the number of elements thermodynamically means raising the entropy of mixing (ΔS_{mix}).

However, it is worth noting that while researchers may be exploring the addition of further elements in Co- or CoNi-based superalloys, they may not have investigated the role of ΔS_{mix} or the principles of HEAs in their design strategies. So it seems that further development of Co- or CoNi-based superalloys must consider the HEAs principles as an essential factor, similar to the development pathway of matured Ni-based superalloys [24]. Overall, the development of Co- or CoNi-based superalloys with advanced properties requires a multidisciplinary approach that combines experimental, theoretical, and computational methods.

The fundamental principle of HEAs is the generation of high configurational entropy, which is primarily achieved by incorporating at least five elements with concentrations ranging between 5 and 35 at%. This criterion was deliberately chosen, as it leads to a solid solution with sufficient entropy to overcome the enthalpy of formation of intermetallic phases, thereby forming a stable solid solution. Research in the past decade has demonstrated that the number of elements in HEAs can be increased up to 13, and the requirement of equal atomic percentages of each element is not essential. Consequently, a new generation of HEAs has emerged, enabling the synthesis of complex multicomponent alloys with enhanced properties [25]. Precisely predicting the stability of solid solutions is a critical factor in developing new HEAs and is of significant interest to the scientific community. Several methods, such as CALPHAD, density-functional theory, and Ab initio molecular dynamics, have been developed to address this issue. However, traditional approaches based on applying Hume-Rothery rules and thermodynamics of phase stability are more suited for practical parametric criteria in predicting the stability of solid solutions in HEAs, as they align well with experimental results [26,27].

In our previous study [28], we introduced a correlation between the entropy of mixing and the solvus temperature of γ'. With some precautions, we found that increasing ΔS_{mix} can positively impact the solvus temperature of γ', and that it is feasible to achieve higher γ' solvus temperatures by increasing ΔS_{mix}. However, a significant increase in ΔS_{mix} can also lead to a higher level of confusion in the alloy system, resulting in a considerable decrease in the Gibbs free energy of mixing (ΔG_{mix}). Consequently, the elements within the alloy tend to randomly distribute themselves in the crystal lattice, which reduces the tendency for ordering and segregation of alloy elements. This phenomenon can lead to the formation of a stable solid solution, which is more favorable than intermetallic compounds or other ordered phases during solidification. Furthermore, the effect of ΔS_{mix} becomes more pronounced as the temperature rises, according to thermodynamic principles. Consequently, a high value of $T\Delta S_{mix}$ can promote the formation of solid solutions. Evaluating the value of $T\Delta S_{mix}$ can help to determine the driving force for forming a solid solution. The approach to designing HEAs is largely dependent on fulfilling a range of thermodynamic prerequisites such as ΔS_{mix}, enthalpy of mixing (ΔH_{mix}), valence electron configuration (VEC), and atomic size difference (δ_r). The probability of forming a single-phase HEA for a given composition can be predicted through analytical calculations of these parameters (and comparing them with statistical ranges) or by employing CALPHAD simulations, which can forecast the phase diagram of a composition across a temperature range [29–31].

The successful development of Co- or CoNi-based superalloys depends not only on the multidisciplinary alloy design strategy but also on the choice of production technique. While conventional ingot metallurgy routes have been widely used in previous studies [8], there is a growing need to focus on sustainable materials that are compatible with advanced manufacturing technologies. Powder technology serves as a gateway to advanced manufacturing technologies, and the production of CoNi-based HESA powders remains an area with limited information. Furthermore, when developing Co-based superalloy powders using powder metallurgy (PM) techniques, elemental segregation can occur during powder production processes such as atomization, which is a common challenge [32]. Therefore, it is essential to consider not only the alloy design but also the production technique in the development of Co- or CoNi-based superalloys suitable for advanced manufacturing.

Modern powder technology provides solutions for advanced and sustainable manufacturing processes, such as PM and additive manufacturing (AM). The mechanical alloying technique is commonly used to produce Co- or CoNi-based superalloy powders, which can then be consolidated using various techniques, including field-assisted sintering techniques (FAST), hot pressing, and spark plasma sintering (SPS) [5,33–38]. Among these techniques, SPS is a PM route for materials processing, which can produce high-dense and low-grain-growth products at relatively low sintering times and temperatures [39–42]. The SPS process has attracted a lot of attention in developing Ni-based superalloys, many of which involve incorporating intermetallic compounds as reinforcements to create metal matrix composites [43–45].

To successfully develop Co- or CoNi-based superalloys, using an accelerated alloy design methodology and selecting the production technique are crucial factors. This study aimed to introduce a novel approach to develop CoNi-based HESA powder through a systematic alloy design strategy. To avoid the precipitation of deleterious secondary phases and segregation during powder production, SPS process, and post-processing heat treatments, CALPHAD calculations and HEAs principles were used in the design step. The validity of the thermodynamical predictions was confirmed in different stages of the manufacturing process, including powder scale (gas atomization), SPS process, solutionizing, and aging. Advanced characterization techniques were used to analyze the microstructural features of the developed powder and consolidated compacts to validate thermodynamic calculations. Moreover, the SPS and heat treatment parameters were optimized based on microstructural assessments and physical and mechanical properties to obtain nearly fully dense materials.

2. Experimental methods

2.1. CALPHAD calculations

The commercially available TCNI11 database in ThermoCalc 2022a software (Solna, Sweden) were utilized to calculate isopleth phase diagrams, mass molar fractions, and solidification curves using the Lever role (equilibrium state) and Gulliver-Scheil classic model (non-equilibrium state). Based on the calculations, an octonary CoNi-based HESA with a nominal composition of Co–35Ni–8Al–4Ti–4V–2Ta–2W–9Cr (at. %) with a high ΔS_{mix} value of 1.568R as our target alloy was selected.

The corresponding powder was produced through Ar gas atomization by CEIT (San Sebastián, Spain, Spain) The powder's characteristics and morphology were analyzed using X-ray diffraction (XRD, Empyrean, PANalytical) and field-emission gun scanning electron microscope (FEGSEM, Apreo 2S, ThermoFisher Scientific), equipped with energy dispersive spectroscopy (EDS) and electron backscattered diffraction (EBSD) detectors (Oxford Instruments).

2.2. Consolidation and heat treatment

After sieving the powder was consolidated via SPS using an HP D 25/3 furnace (FCT System, Germany) in a 20 mm cylindrical graphite die at various temperatures (1150 °C and 1175 °C), holding times (5–10 min), and heating rates (100 and 400 °C.min^{-1}) with an applied compaction pressure of 50 MPa in a vacuum. The density of the SPS processed samples was measured using the Archimedes method, according to ISO 18754 standard.

Solution and aging heat treatments on the optimized SPS samples were performed. To explore the effect of heat treatment parameters, we designed experiments based on the cooling medium after solutionizing and aging temperature. For quenching after solutionizing at 1190 ± 10 °C for 2 h, we selected air and water mediums. The solutionized samples were aged at 800 °C, 900 °C, and 1000 °C for 24 h, followed by water quenching.

2.3. Characterization

To investigate the microstructural characteristics of the samples,

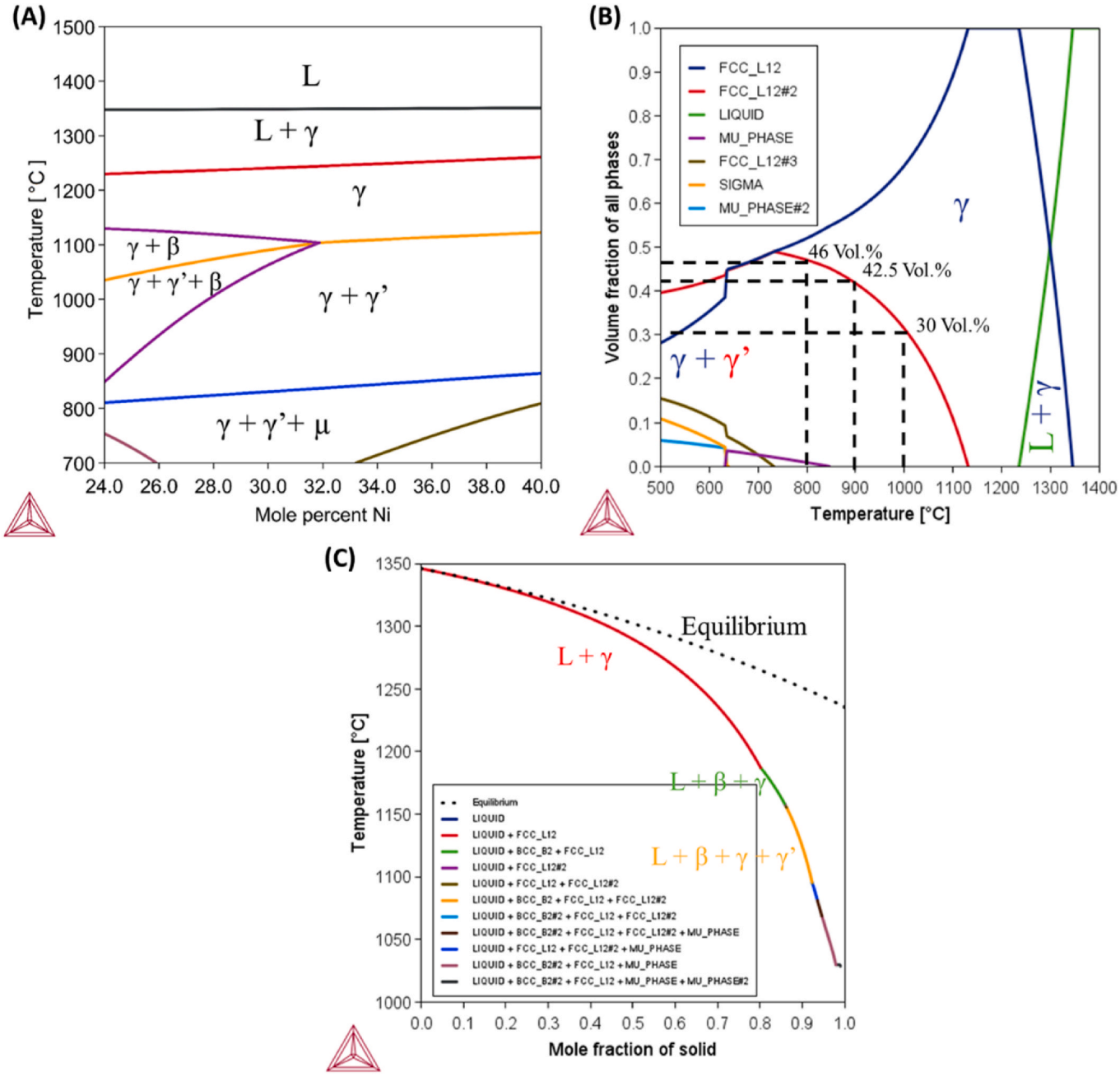


Fig. 1. CALPHAD calculations of the developed CoNi-based HESA using different approaches: (A) calculated isopleth section of XCo-YNi-8Al–4Ti–4V–2W–2Ta–9Cr (at. %) showing the variation of Ni at the expense of Co; (B) phase diagram of alloy Co–35Ni–8Al–4Ti–4V–2W–2Ta–9Cr (at. %); and (C) solidification pathway of Co–35Ni–8Al–4Ti–4V–2W–2Ta–9Cr (at. %) based on the Scheil solidification model.

cross sections of the SPS-processed, solutionized, and aged materials were prepared by first mechanically grinding and polishing the surfaces to a 1 μm grit size using a series of diamond pastes. The final polishing step was then carried out using the oxide polishing suspension (OPS) technique, which involved using a 40 nm colloidal silica suspension to achieve a smooth and flat surface for analysis. The relative density (RD) and γ' percentage values were determined from optical microscope (OM, Olympus BX51) and high resolution SEM images using the ImageJ software [46], respectively. Kalling etchant reagent was used to etch all samples for 20–30 s after final polishing by the OPS solution. The EBSD micrographs were collected on the powder cross-section and SPS processed parts as well as the solutionized samples, with a step size of 0.5–0.7 μm, an accelerating voltage of 20 kV, and a beam current of 3.2 nA. The AZtecHKL acquisition software was used for imaging and orientation data analysis. The Vickers microhardness was conducted using the INNOVATEST instrument by applying a 1 kg load and a 10 s dwell time at room temperature. At least three measurements were taken to determine the average hardness values. Micro-tensile samples with dog-bone shapes were prepared using electro-discharge machining (EDM). The samples had a central section measuring 4 mm in length and 1 mm in width. Tensile tests were conducted at room temperature using a 10 kN micro-tensile testing machine from Kammrath and Weiss, following the guidelines outlined in ASTM E8/E8M [47]. At least two tests were taken to determine the average tensile properties.

3. Results and discussion

3.1. Assessing segregation and TCP phase formation through CALPHAD and HEAs calculations

Building on previous research by the authors [28], segregation and the formation of TCP phases during the atomization, spark plasma sintering (SPS), and heat treatment processes of a 36Co–35Ni–8Al–4Ti–4V–2Ta–2W–9Cr (at. %) alloy was further investigated. Fig. 1A depicts the isopleth section of XCo-YNi-8Al–4Ti–4V–2W–2Ta–9Cr (at. %) plotted against Ni variation at temperatures ranging between 700 and 1500 °C, with other elements kept constant. It can be seen that by increasing Ni content, the β phase zone decreases, and γ' solvus temperature increases. Lass [20] reported the formation of a β phase bubble in a Co–Ni–Al–W system using the TCNI8 database, which has not been experimentally confirmed. Liang et al. [48] also suggested that the formation of β phase in a high-Cr CoNi-based superalloy, using the TCNI8 database, is related to the Cr and Ni contents. They concluded that to avoid β and σ phase formation, the Cr content should not exceed 20 at. %. Balancing Co and Ni concentrations is essential for achieving the highest ΔS_{mix} value. According to Fig. 1A, the Ni content can be increased up to 35 at. % without formation of β phase. Therefore, we selected an alloy with 36 at. % Co and 35 at. % Ni with $\Delta S_{mix} = 1.568R$ for further investigation. The phase diagram of the selected composition Co–35Ni–8Al–4Ti–4V–2W–2Ta–9Cr is presented in Fig. 1B, which indicate the potential formation of μ and σ phases at temperatures below ~850 °C and ~650 °C, respectively. Thus, there is a broad range of possible heat treatment temperatures above 850 °C.

In the non-equilibrium state (atomization process), the solidification pathway of the selected alloy was investigated, and the result is shown in Fig. 1C for the Co–35Ni–8Al–4Ti–4V–2W–2Ta–9Cr composition. The solidification curves reveal the thermal history of the alloy during solidification and provide valuable information about the formation of different phases. Upon analysis of the solidification curves, there is a narrow temperature range of between 1150 and 1200 °C, where the formation of β phase takes place. This suggests that controlling the solidification is crucial to obtain the desired phase composition and microstructure. In addition, the formation of the β phase is dependent on the alloy composition, with a higher Ni content leading to a decrease in the β phase zone, as discussed earlier. Overall, understanding the solidification pathway and the temperature range for the formation of different phases is essential for controlling the microstructure and properties of the alloy.

The CALPHAD calculations have determined that a single-phase solid solution can be obtained at a temperature above 1150 °C in the equilibrium state and 1200 °C in the NE state. The cooling during solidification and even heat treatment will play a significant role in controlling the phase transformation. Therefore, controlling the cooling rate will be crucial in achieving the desired microstructure and properties.

The selected composition's ΔS_{mix} value of $1.568R$ indicates that incorporating eight elements will increase degree of randomness, lattice distortion, and lead to sluggish diffusion, which may affect the experimental results [49]. The incorporation of multiple elements with different atomic sizes makes it difficult for atoms to diffuse to their intended positions, slowing down diffusion (sluggish diffusion). As a result, the material's synthesis and processing conditions must be carefully controlled to minimize the formation of unwanted phases.

In the design of HEAs, various thermodynamic parameters need to be considered to predict phase formation and stability. One important parameter is the atomic size difference parameter (δ_r), which has been found to be particularly effective in predicting the formation of intermetallic phases and phase separation in HEAs [49,50]. This is because when there is a high misfit in atomic size between different elements, it leads to significant lattice strain, which can result in phase instability and the formation of intermetallic compounds.

The δ_r value is a measure of the degree of deviation from ideality in a solid solution. A value higher than the critical value of 6.6 % indicates that the solid solution is not random, and there is a tendency towards phase separation. In contrast, a δ_r value lower than the critical value suggests that the solid solution is random, and that phase separation is not likely to occur. The δ_r parameter can be calculated using the following equation:

$$\delta_r = 100\% \sqrt{\sum c_i (1 - r_i/\bar{r})^2}$$

Here, c_i represents the atomic fraction of the ith element in the alloy, r_i is the atomic radius of the ith element, and $\bar{r}$ is the average atomic radius of the alloy ($\bar{r} = \sum c_i r_i$). For the Co–35Ni–8Al–4Ti–4V–2W–2Ta–9Cr alloy, the δ_r value has been calculated to be 5.46 %, which is lower than the threshold value of 6.6 %. This suggests that after solidification, a random solid solution is expected to be obtained rather than phase separation or intermetallic formation.

3.2. Powder characterization

Fig. 2 presents detailed information on the characterization of the CoNi-HESA powder utilized in the study. In Fig. 2A, the morphology of the gas-atomized powder is displayed, showcasing near-spherical particles, with some small satellites, and a particle size distribution with values of $D_{10} = 52.5$ μm, $D_{50} = 76.6$ μm, and $D_{90} = 117.0$ μm. To gain insight into the powder's structure and composition, Fig. 2B-C-D depicts the results of XRD, EBSD, and EDS analyses, respectively. These analyses reveal a single-phase FCC crystal structure with a small amount of BCC phase (0.6 %), indicating the micro-segregation of Ti and Ta without the formation of TCP phases during the rapid solidification process employed in gas atomization. Solidification segregation is a common challenge encountered during the atomization process of CoNi-based superalloys according to Knop et al. [38]. This phenomenon refers to the non-uniform distribution of alloying elements within the solidified material. It occurs due to variations in the cooling rates and solute partitioning during solidification, leading to the formation of localized regions enriched or depleted in certain elements.

Based on the solidification pathway in the NE state (Fig. 1C), the formation of the β phase is possible. In order to confirm whether the detected small amount of BCC phase corresponds to the β phase, the elemental distribution of Co, Ni, Al, Ti, and Cr from the EBSD map of the powder cross-section is presented in Fig. 3. Notably, Al and Ti exhibit significant contributions within the BCC area, and their distribution

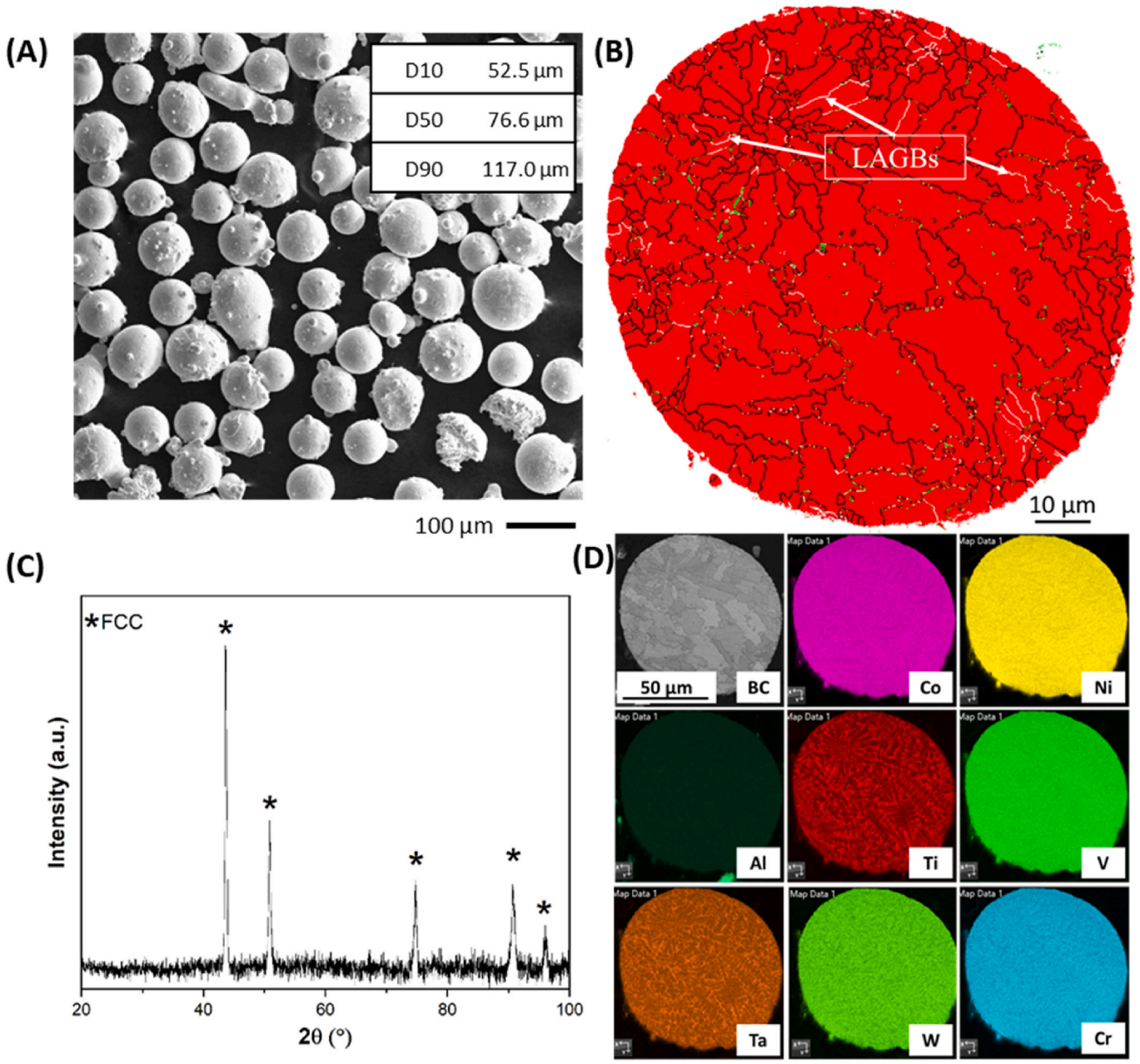


Fig. 2. (A) SEM micrograph of the gas atomized powder showing spherical morphology with a few satellites on each particle. The particle size distribution was added as an inserted table, (B) EBSD phase map and grain boundary analysis of powder cross-section, (C) XRD pattern, and (D) EDS elemental mapping collected on the prepared gas atomized powder (EBSD and EDS collected simultaneously).

aligns well with the BCC phase map. As discussed in Section 3.1, the precipitation of the β phase is influenced by the content of Cr and Ni. Additionally, the formation of the β phase is strongly influenced by the content of Al and Ti, with Ti playing a key role in promoting the precipitation of the β phase from Al. The addition of Ti effectively encourages the formation of the β phase, resulting in its increased presence in the alloy [51,52]. Wen et al. [53] reported the formation of the β phase in both as-solidified and aged conditions for a CoNi-based superalloy with 6 at. % Cr and 13 at. % Al, indicating that a higher amount of Al can directly lead to the precipitation of the β phase. Moreover, the addition of Ni can expand the γ+γ′ region (as shown in Fig. 1A), allowing for higher amounts of these elements to be incorporated [15]. The expansion of the γ+γ′ region facilitated by Ni addition also enables an increase in Cr content [22].

Table 1 displays the chemical composition of the gas-atomized powder, collected at the cross-section of particles, as determined by EDS analysis. The composition closely aligns with the nominal composition of the CoNi-based HESA developed using ThermoCalc. However, there are slight differences observed for Al, Ti, and Ta between the nominal values and the measured values for the powder. These discrepancies may be attributed to micro-segregation effects and the formation of oxides and nitrides during the atomization process.

Upon examining the chemical analysis of the SPSed sample, it is evident that the elemental values are relatively uniform. However, there is still a 1.2 at. % difference observed for Ti compared to the nominal value. This difference can be attributed to the formation of nitrides, as will be discussed later. Furthermore, the actual value of ΔS_{mix}, determined from the EDS results for both the powder and the consolidated HESA sample, is found to be 1.602R and 1.558R, respectively. The consolidated sample demonstrates a ΔS_{mix} value that closely matches the

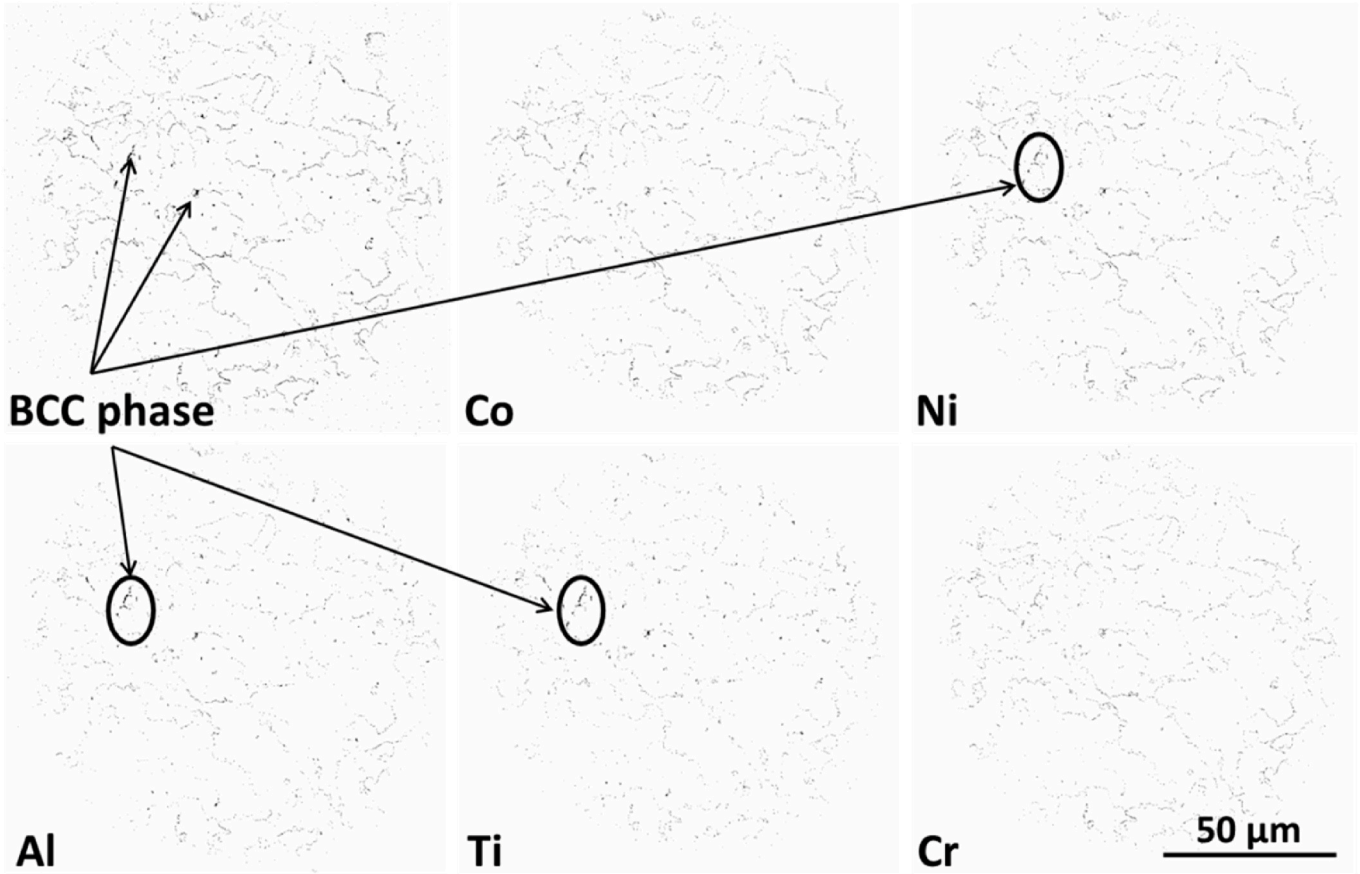


Fig. 3. Elemental Distribution in the BCC Phase. The data was obtained from EBSD results of the powder cross-section, with the exclusion of the FCC phase in order to specifically detect and analyze the distribution of elements in the BCC phase.

Table 1
The nominal and experimental (measured by EDS analysis) chemical composition of the gas-atomized powder in conjunction with their ΔS_{mix}.

	Chemical composition (at. %)								ΔS_{mix}
	Co	Ni	Al	Ti	V	W	Ta	Cr	
Nominal	36	35	8	4	4	2	2	9	1.568*R*
Powder	35.7 ± 1.5	35.4 ± 0.5	7.4 ± 0.3	3.2 ± 1.2	4.1 ± 0.1	2.2 ± 0.4	3.2 ± 1.2	9.4 ± 0.2	1.602*R*
SPS - C	36.1 ± 0.11	35.5 ± 0.08	7.3 ± 0.04	2.80	4.3 ± 0.04	2.2 ± 0.04	2.4 ± 0.04	9.4 ± 0.04	1.558*R*

nominal value, indicating a close alignment with the desired composition.

3.3. Consolidation process by SPS

The experimental layout of the applied SPS process at different times, temperatures, and heating rates is reported in Table 2. Based on the bulk density and relative density measurement results, the maximum densification without open porosity was achieved in sample *C*, sintered at 1175 °C for 10 min with a heating rate of 100 °C.min^{-1}. The schematic of the SPS process and applied sintering profile for sample C is plotted in Fig. 4A and B. During the SPS process, the extent of sintering shrinkage of the powder can be tracked and measured through the displacement curve, where a positive displacement value corresponds to the shrinkage of the system. The SPS process can be divided into five segments: vacuum creation, pressing, heating, holding, and cooling. In the first 3 min and 48 s vacuum was created, and the load was increased to 5 kN, which is the minimum value required for achieving good electrical contact between electrodes and tool setup. Subsequently, in the pressing segment, the load was further increased to 16 kN, resulting in a compaction of the powder. By heating, the tool setup expands up to ≈10 min and 42 s (≈915 °C), where the shrinkage by powder sintering

Table 2
Design layout of the SPS process parameters, as well as the measured bulk and relative density of the SPS processed HESA samples. The applied pressure was 50 MPa.

Sample	Temperature (°C)	Heating time (min)	Heating rate (°C/min)	Density (g/cm^3)	Open porosity (%)	Relative density (%)
SPS-A	1150	10	100	8.55	0.2	99.84 ± 0.12
SPS-B	1150		400	8.53	0.2	99.72 ± 0.17
SPS-C	1175		100	8.56	0.0	99.90 ± 0.04
SPS-D	1175	7	100	8.53	0.0	99.41 ± 0.27
SPS-E	1150	15	400	8.52	0.1	99.59 ± 0.38

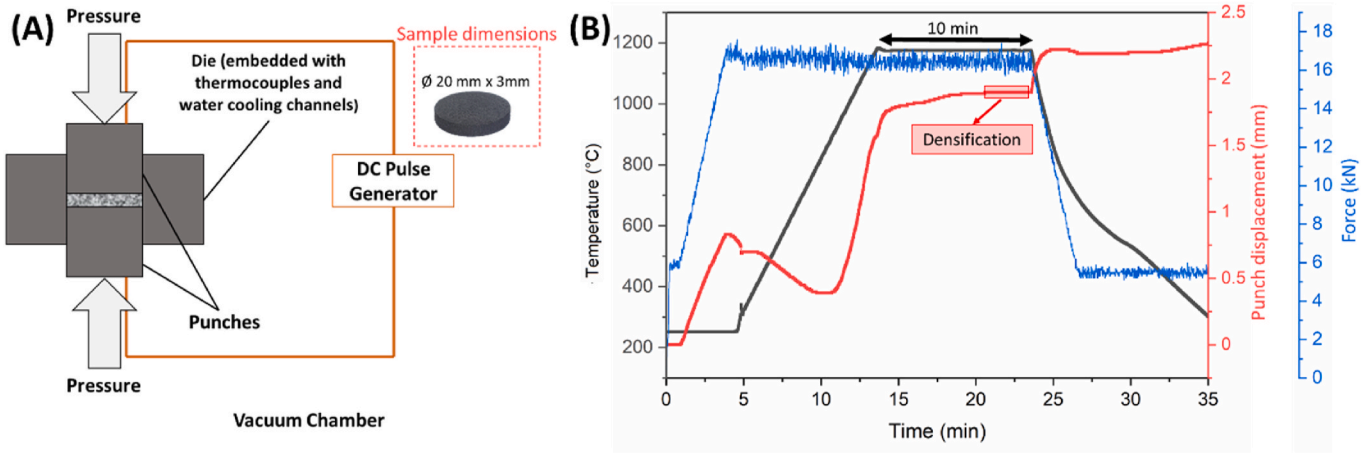


Fig. 4. (A) Schematic of the SPS configuration and pellet dimension. (B) The piston displacement, load, and temperature against time for consolidation of the CoNi-based HESA powder SPS processed at 1175 °C for 10 min with a heating rate of 100 °C.min^{-1} under an applied pressure of 50 MPa.

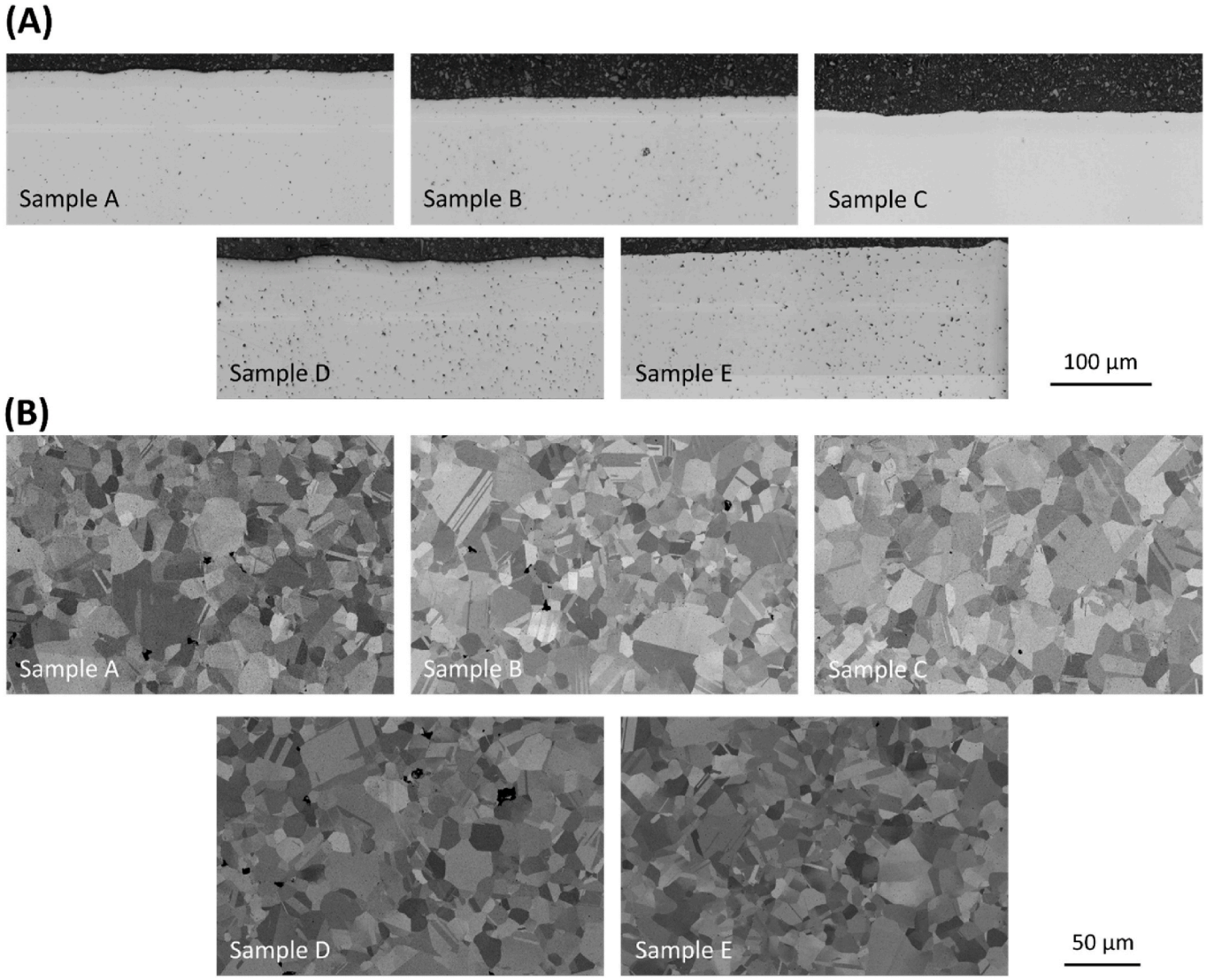


Fig. 5. (A) Optical micrographs at the cross-section of SPS samples showing porosity. (B) Backscattered SEM micrographs of the SPS processed HESA at different processing conditions.

exceeds the thermal expansion. After 13 min and 30 s (1175 °C), the sintering starts, and after 20 min and 30 s, densification is completed, and the additional holding time at 1175 °C does not induce extra shrinkage.

3.4. Microstructure observation of SPS processed HESA

Optical and scanning electron microscopy - The optical images (Fig. 5A) and backscattered SEM micrographs (Fig. 5B) of the SPS processed samples at different conditions were used to analyze porosity and grain structures after consolidation. The optical micrographs showed porosity distribution where sample C had the lowest remnant porosity in the consolidated part. Also, it is seen that there was a homogeneous distribution of the grains in all samples. Based on the SPS processing condition, remnant pores were also seen on the SEM micrographs supported by the relative density measurements. To assess the potential reason for remnant porosity in the final SPS processed parts, the SPS process optimization strategy was elaborated.

At first, based on the isopleth phase diagram calculation shown in Fig. 1A, powders were sintered at 1150 °C for 10–15 min at different heating rates of 100 and 400 °C.min^{-1}. The Micrographs for samples B and E showed irregular remnant pores at the grain boundaries, which meant that the prolonged SPS did not assist with pore removal. Considering the heating rate at a constant sintering time (10 min) and temperature (1150 °C), for instance, samples A (heating rate of 100 °C.min^{-1}) and B (heating rate of 400 °C.min^{-1}), it was noticed that there was more evidence of incomplete sintering. Thus, a higher heating rate results in a lower relative density and more porosity with irregular morphology. The SPS consolidation temperature was increased to 1175 °C with a constant heating rate of 100 °C.min^{-1} at two dwell times of 7 min (sample D) and 10 min (sample C). When the dwell time was 7 min, based on the time vs. displacement curve in Fig. 4B, the SPS consolidation cycle is very close to the starting point of the complete densification. Hence, lower sintering time can describe highly

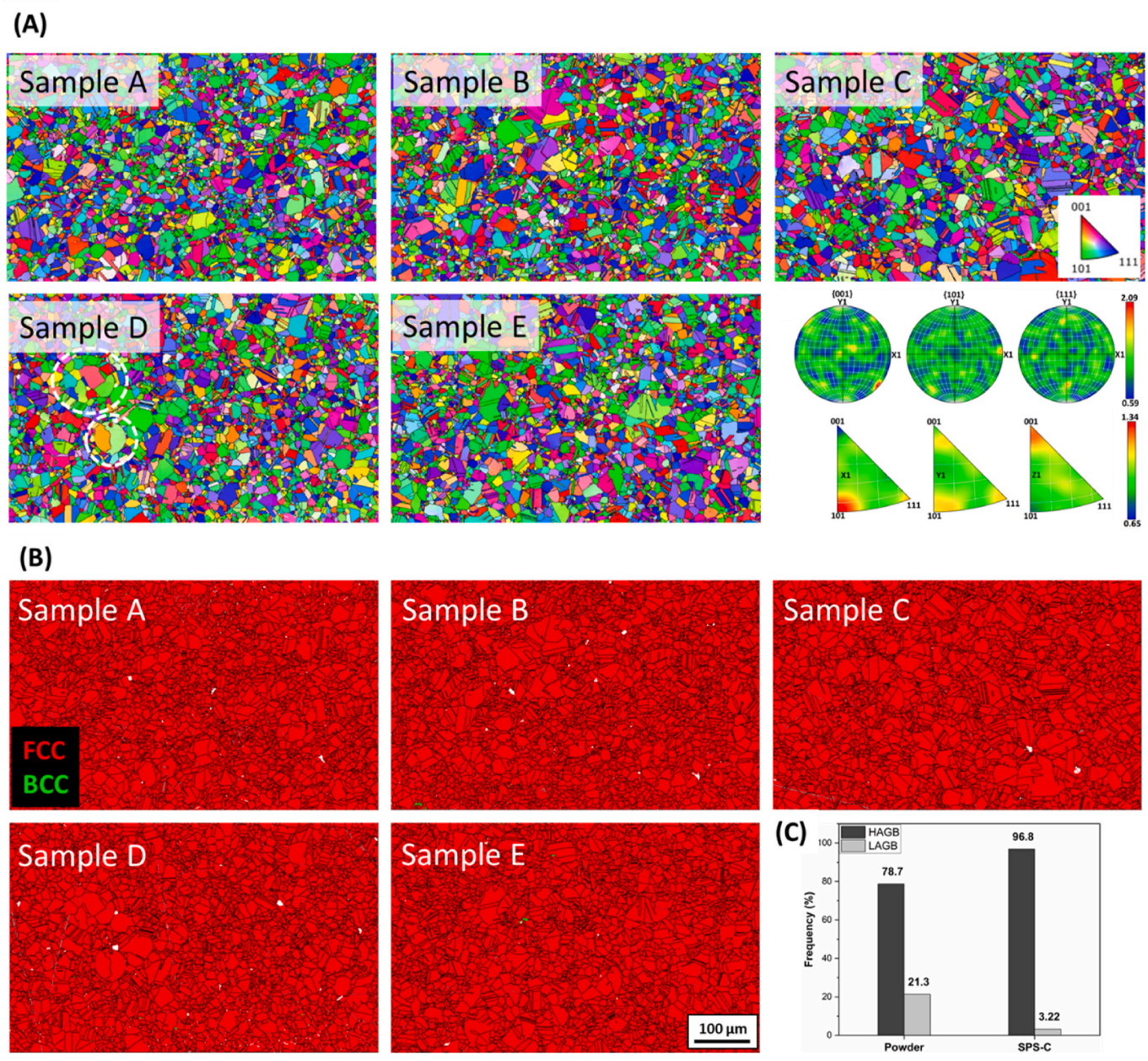


Fig. 6. EBSD micrographs from the SPS processed CoNi-HESA, (A) IPF-Z maps and pole figure, (B) phase maps and grain size analysis, (C) typical LAGBs (2–15°) and HAGBs (>15°) analysis of powder and SPSed sample C.

populated, irregular pores in sample D compared to sample C. Thus, the optimum SPS cycle, shown in Fig. 4B, resulted in the highest relative density of 99.9 %.

Texture and phase analysis – The EBSD analysis was carried out to characterize texture, grain size and phase fraction of FCC and BCC and the results are shown in Fig. 6. Inverse pole figure (IPF-Z) maps (Fig. 6A) shows grain crystallography and twinning. During SPS process, a uniaxial pressure is applied on powder, however, no evidence of a strong texture was seen in the EBSD maps of the SPS processed samples in the applied pressure direction (height or Z-direction), and equiaxed grains (see pole figure map) with minimal grain growth due to short processing time at elevated temperatures was observed. When the dwell time at maximum temperature is low, there is a possibility for incomplete sintering, as evident in Fig. 6A and sample D. Specifically, two areas were detected (white, dash circles) on the EBSD IPF-Z map in which the starting powder with diameters of 63–100 μm trapped within the matrix. This occurrence can be attributed to the incomplete diffusion process required for neck growth. When the diffusion process is not fully completed, the particles retain their original diameter and shape, thus remaining unchanged within the final product.

Fig. 6B illustrates the EBSD phase maps obtained from the SPS processed samples. Referring to the solidification curve in the NE state ((Fig. 1C), there is a possibility of β phase formation at temperatures of 1150 °C and 1175 °C. However, the EBSD results reveal a single phase FCC crystal structure with a fraction of ~99.9 %. Comparing these findings with the CALPHAD results in the equilibrium state (Fig. 1A and B) and the EBSD phase maps, it can be inferred that successful consolidation via SPS resulted in the formation of a single FCC phase HESA material.

Fig. 6C presents the fraction of low-angle grain boundaries (LAGBs) and high-angle grain boundaries (HAGBs) in both the atomized powder and the SPS processed sample C. LAGBs are defined as grain boundaries with angles between 2 and 15°, while HAGBs have angles greater than 15°. The analysis reveals that the atomized powder initially possesses a significant amount of LAGBs, accounting for 21.3 % of the total grain boundaries (as shown by arrows in Fig. 2B). However, after undergoing the SPS process, the proportion of LAGBs decreases substantially to 3.22 %. Post-SPS, the majority of the grains are associated with HAGBs. In the case of sample C, approximately 96.8 % of the grain boundaries fall into the HAGB category. This suggests that the consolidation process resulted in the formation of grains with larger sizes and a greater prevalence of HAGBs, indicating localized recrystallization and grain growth.

Elemental analysis - Elemental analysis using EDS mapping was employed to study possible precipitation of unwanted secondary phases or intermetallic compounds at the grain boundaries. Fig. 7 shows the elemental analysis, grain boundaries, and γ/γ' distribution of the SPS processed sample B. In Fig. 7a, it is apparent that no precipitates were present at the grain boundaries and there were no topologically closed packed (TCP) phases, in agreement with our thermodynamic calculation. The small dots observed in the Ti and nitrogen N maps correspond to the presence of Ti-rich nitride. These nitrides are primarily a result of the melting process that occurs during atomization. In Fig. 7a-c with higher magnification of the SEM micrographs, a uniform and fine γ' distribution was observed. As an advantage of the SPS process, the grain structure remains small, close to the one characteristic of the powder feedstock. Thus, homogenization and solutionizing of the CoNi superalloy at a short dwell time can minimize grain growth which could be beneficiary to the mechanical properties. Finally, it should be taken into account that the FCC phase within the microstructure contains disordered FCC (γ) and ordered FCC (γ') phases (see Fig. 7c).

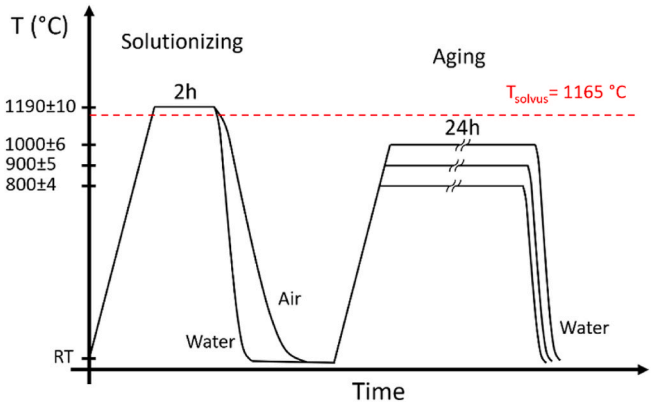


Fig. 8. Heat treatment cycles including solutionizing and aging.

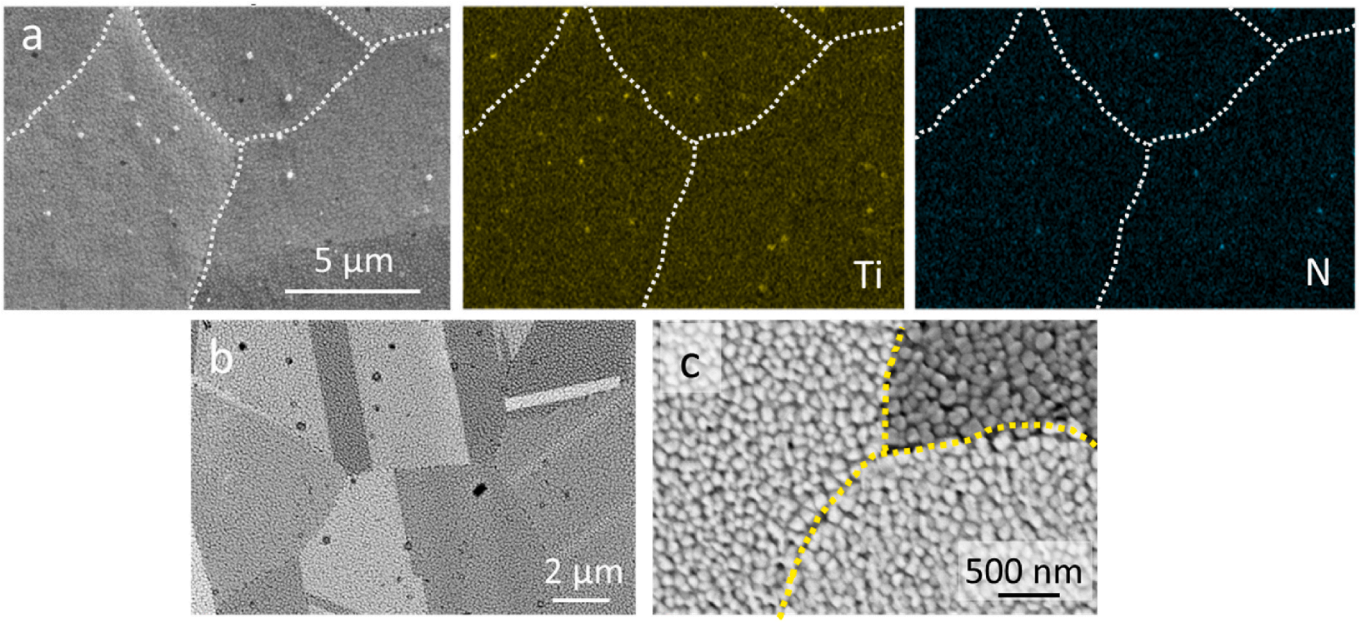


Fig. 7. (a) Elemental analysis using EDS map of sample B, and (b,c) backscattered SEM micrographs from the grain boundaries of sample B. Grain boundaries are shown using dash lines.

3.5. Analysis of heat treated SPS processed CoNi-HESA

The heat treatment cycles were applied to sample C, as shown in Fig. 8. Drawing from our previous experience with the solvus temperature of the γ' phase in the alloy composition and CALPHAD calculations, a solutionizing treatment was conducted at 1190 ± 10 °C for 2 h, followed by rapid cooling through water quenching and standard cooling via air quenching. Subsequently, the solutionized samples underwent aging at temperatures of 800 °C, 900 °C, and 1000 °C for 24 h to validate the accuracy of the CALPHAD calculations for the developed CoNi-based HESA. Since the isopleth section and phase diagram are plotted under equilibrium conditions, it becomes crucial to validate the CALPHAD predictions after subjecting the samples to heat treatments that bring them closer to the equilibrium state. These heat treatments serve to validate the accuracy of the CALPHAD calculations and verify their applicability in predicting the phase transformations and microstructural evolution in the developed CoNi-based HESA material.

Microstructure observations of the solution heat-treated CoNi-HESA - In Fig. 9A, the EBSD IPF-Z and phase maps of solution heat-treated (SHT) samples are shown. No significant grain growth was observed in the SHT samples, as demonstrated in Fig. 9B, compared to the SPS-processed ones. Equiaxed grains with a uniform size distribution were observed. The grain size of the gas-atomized powder was measured to be 3.5 ± 2.7 μm, which increased to 7.2 ± 5.1 μm in sample C. When the samples were solution-treated followed by water and air cooling, the average grain size remained almost unchanged at 6.9 ± 5.1 μm and 8.4 ± 5.5 μm, respectively. Cao et al. [19] reported a significant grain growth in a W-free Co-based superalloy produced by casting, cold rolling followed by solutionizing at 1200 °C with a final mean grain size of 38 ± 5 μm. One main advantage of the SPS process is quick consolidation leading to the formation of fine grain structured products.

The phase map results collected on the SPS processed parts showed less than 0.1 % BCC phase in the microstructure which could also be considered as noise. After SHT, it was seen that the fraction of the BCC phase (green color) slightly increased to 0.2 % (water-quenched) and 0.5 % (air-quenched). According to the isopleth phase diagram shown in Fig. 1A, a wide temperature range exists (~1100–1240 °C) for solutionizing the designed composition to obtain a single phase FCC structured alloy. The presented EBSD phase maps of the solutionized samples validated the thermodynamic calculations, and the microstructure was mainly a single-phase FCC structure. To better understand the nature of the detected BCC phase, the EDS detector was inserted simultaneously with the EBSD detector in the case of the water-quenched sample. Regarding the elemental analysis using EDS mapping (see Fig. 9C), the only possible BCC phase that might be formed based on the isopleth phase diagram is the β phase rich in Al and Ti. No TCP precipitations

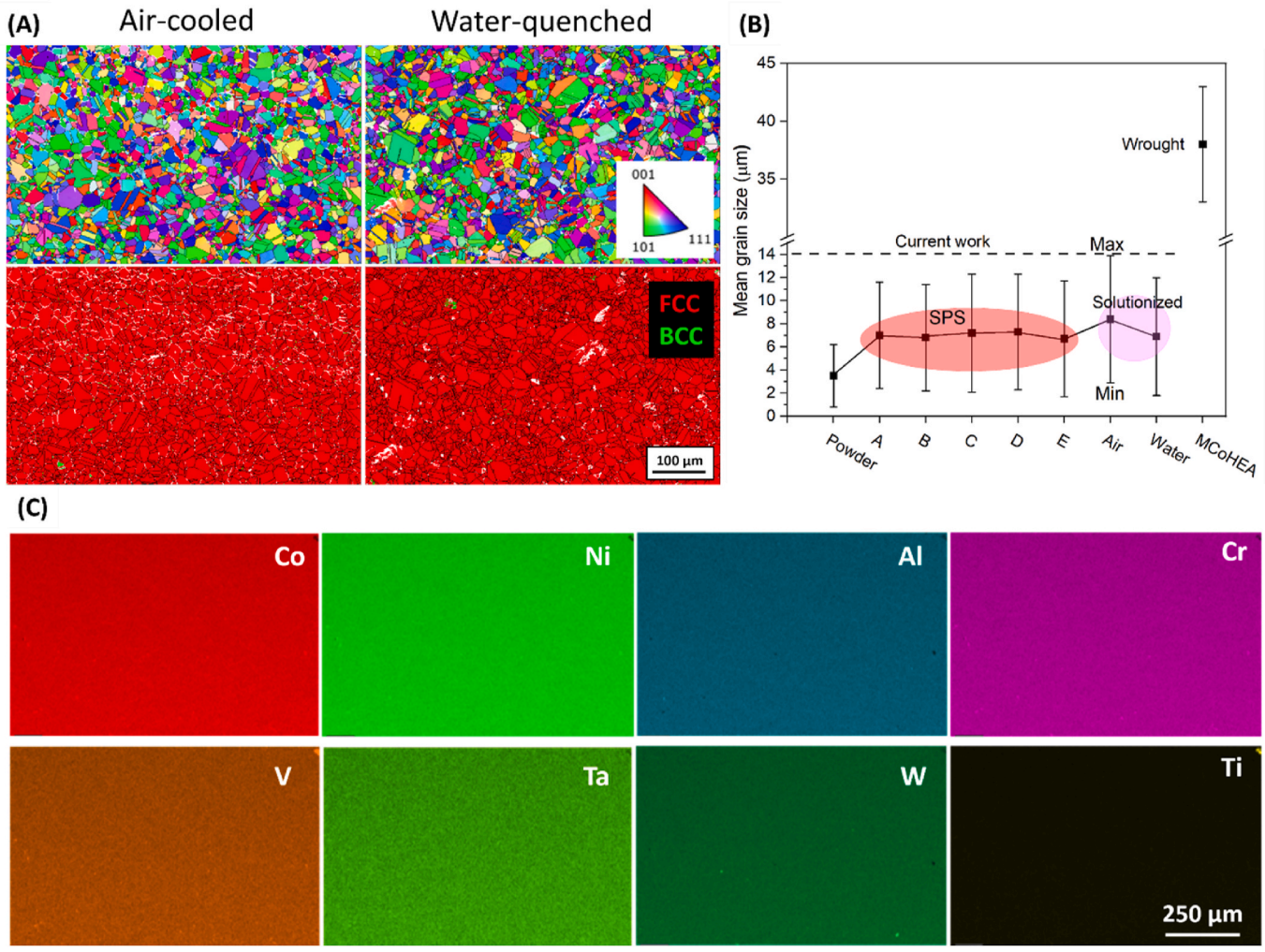


Fig. 9. (A) EBSD micrographs from the SPS processed HESA sintered at 1175 °C for 10 min with a heating rate of 100 °C.min^{-1} (sample C). (top) IPF-Z maps and (bottom) phase maps and grain size analysis results. Samples were solutionized 1190 ± 10 °C for 2 h followed by air-cooling or water-quenched conditions. (B) Analysis of mean grain size in the used gas atomized powder, SPS processed samples, and solutionized specimens. Results were compared with wrought Co-based HESA [19]. (C) Elemental analysis using EDS mapping of the SPS processed sample after solutionizing followed by water cooling. Results were collected on the same area in which the EBSD data was collected.

were detected in the indexed area, and the matrix was mainly an FCC solid solution structure.

Microstructure observations of the aged HESA – To further improve the mechanical properties of the solution heat treated samples, aging treatment was applied. Fig. 10 shows backscattered electron SEM micrographs of samples aged at different temperatures. Regardless of the SHT process (being air-cooled or water-quenched), the microstructure showed a fine grain structure. Also, no notable grain growth as well as the secondary and TCP phases were seen. To evaluate the impact of aging temperature on morphology, size, and distribution of γ/γ', SEM micrographs at higher magnification were collected. After etching with the Kalling solution, the black areas are associated with γ phase, and the white areas correspond to γ' phase. Comparing the microstructure of the aged samples as a function of cooling conditions after SHT, it was found that the size of the γ' phase was slightly bigger in the air-cooled sample compared to the water-cooled sample (particularly aged at a lower temperature, i.e., 800 °C). Also, the size of γ' precipitates increased with increasing aging temperature. In terms of the shape, γ' precipitates with round morphology formed in the microstructure of the ages samples. Interestingly, a prolonged aging treatment at 1000 °C for 24 h resulted in no precipitate formation, i.e., TCP phases, at the grain boundaries. To validate our observations as well as the CALPHAD prediction, elemental analysis was performed using EDS mapping at the grain boundaries and results were shown in Fig. 11. TCP phases, such as μ and σ phases, can occur in CoNi-based superalloys, and their presence can significantly degrade the creep properties of these alloys [36]. In a study by Zhuang et al. [22], a septenary CoNi-based superalloy was developed using the CALPHAD method with the PanCo database, but the formation of TCP phase rich in Ti, W, and Ta (μ phase) was observed despite not being predicted in their calculations. In another work by Liang et al. [37], high-Cr CoNi-based superalloys were developed using the TCNI8 database in their calculations. They reported the formation of σ phase in Co–30Ni–30Cr–5Al–5Ti (at. %) by CALPHAD prediction and experimentally observed it after aging at 900 °C for 220 h. Our calculations suggest that the formation of μ and σ phase is possible at temperatures lower than ~850 °C, as indicated by the phase diagram (Fig. 1B). Given the possibility of μ phase formation at temperatures lower than ~850 °C, it is noteworthy that our results did not show any evidence of its

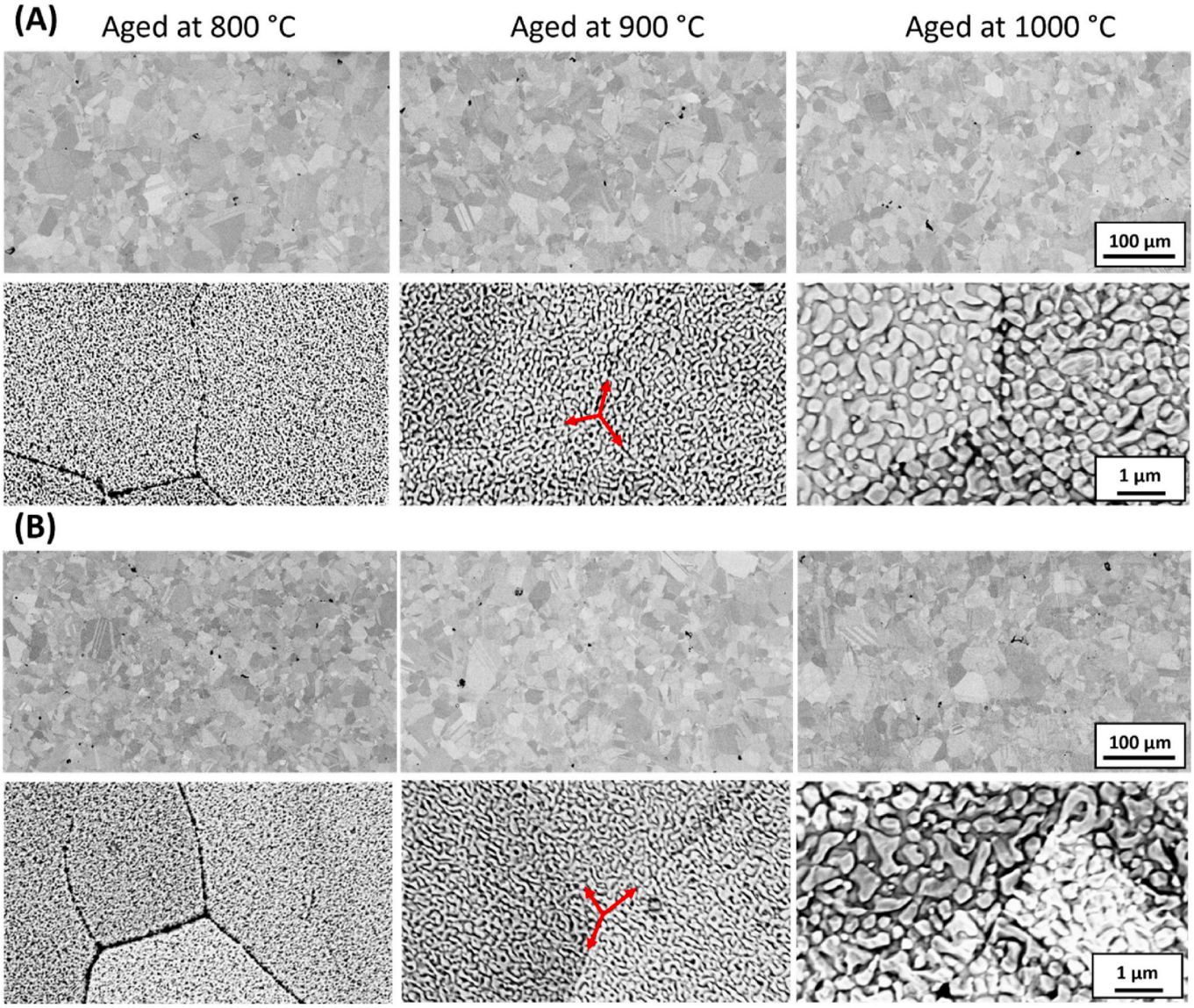


Fig. 10. Backscattered electron SEM micrographs collected from the (A) SHT sample and air-cooled and (B) SHT sample and water-quenched, both followed by aging treatment at different holding temperatures. Micrographs with two magnifications were presented to observe grain structure (low magnification), and γ/γ' interface and their distribution (high magnification). After the SPS, sample C was selected as an optimized consolidated condition for additional heat treatment including solution treatment (air-cooled or water-quenched and aging followed by water-quenching.

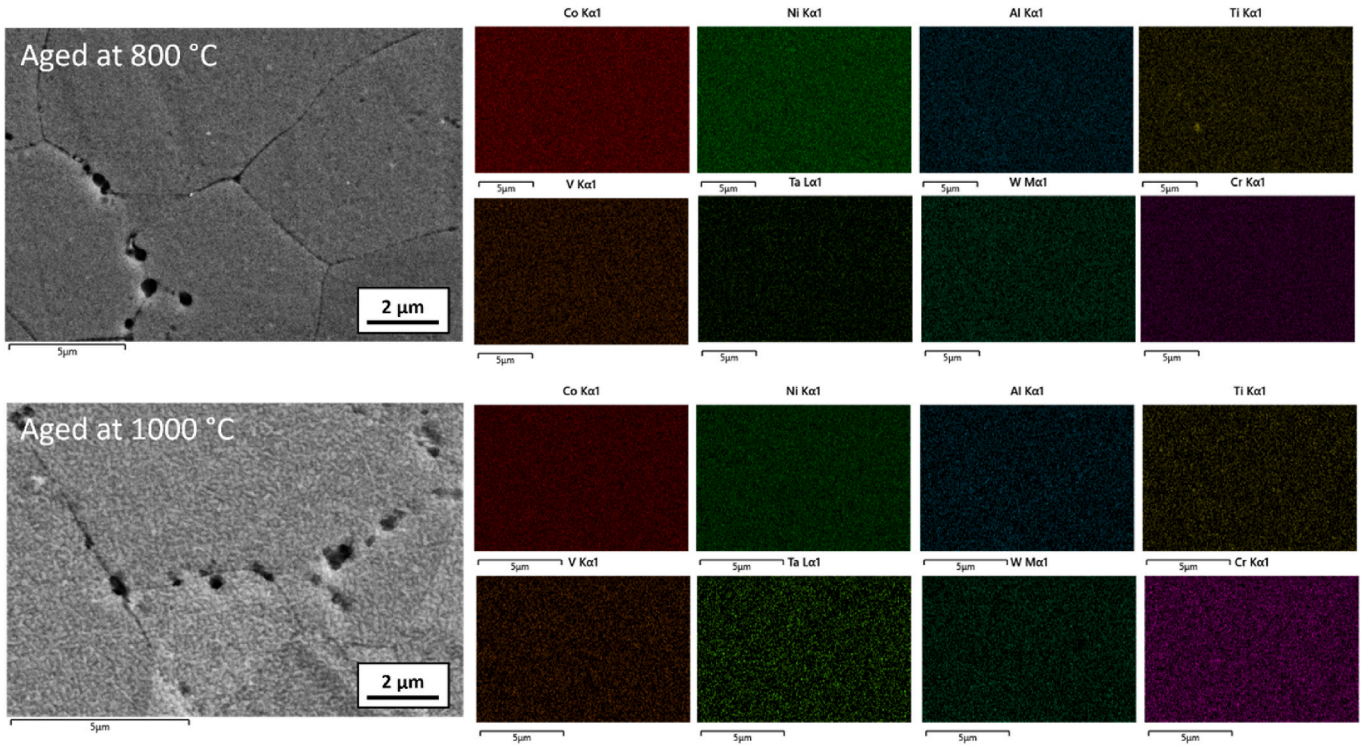


Fig. 11. EDS elemental analysis at the grain boundaries of the SHT sample C followed by air-cooling, then aged at two temperatures for 24 h.

formation under these conditions. Therefore, we can conclude that sluggish diffusion and random solid solution result from high entropy and small misfit. The complex chemical composition, intentionally designed to promote the "cocktail effect," effectively controls phase stability and prevents the formation of deleterious secondary phases and TCP phases along the grain boundaries [49,54–56]. This phenomenon can be attributed to the presence of eight elements in an FCC crystallographic structure, which results in a ΔS_{mix} value of 1.558*R*.

According to the phase diagram analysis presented in Fig. 1B, the volume fraction of γ' is predicted to vary at different temperatures. At 800 °C, the maximum predicted amount of γ' is approximately 46 %. However, the calculated fraction of γ' for the air and water cooled samples is 68.69 ± 0.97 % and 72.61 ± 2.55 %, respectively. These experimental values indicate a higher fraction of γ' compared to the predicted value. As the aging temperature increases, the fraction of γ' decreases to 65.17 ± 12 % and 65.45 ± 0.49 % for the air- and water-cooled samples, respectively. At 900 °C, the predicted value for the γ' fraction is 42.5 %, which does not align well with the CALPHAD prediction. However, it is important to note that the trend observed in both the predicted and experimental values remain consistent, as the γ' fraction decreases with an increase in aging temperature.

3.6. Mechanical properties

Microhardness measurements – Vickers microhardness measurements were carried out on the developed CoNi-based HESA, and results

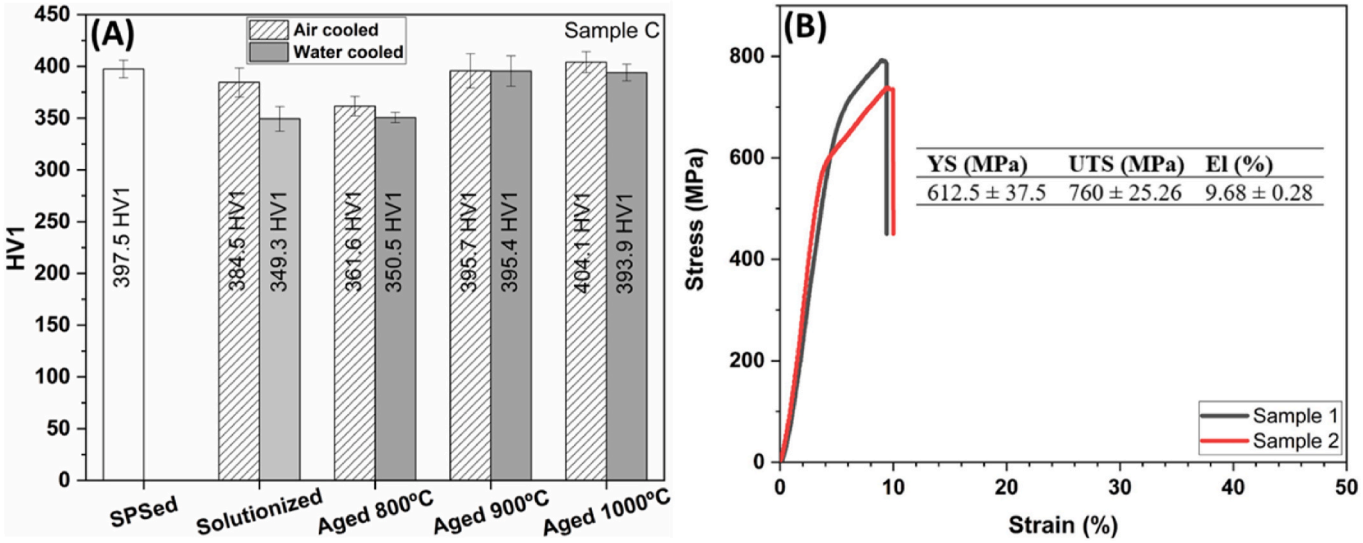


Fig. 12. (A) Vickers microhardness measurements on the SPS processed sample C, solutionized and differently aged HESA. (B) Engineering stress–strain curve of SPSed sample C subjected to SHT + WQ and aged at 900 °C followed by water quenching.

are shown in Fig. 12A. The microhardness of the SPS processed sample was 397.5 HV_1, in agreement with the previously reported values in the family of CoNi-based superalloys [23,57]. After solutionizing followed by water-quenching, the microhardness value decreased more than the air-cooled sample. In other words, the microhardness of the air-cooled sample was very close to the SPS processed one, meaning that the air-cooling condition might not be an appropriate pathway to attain a supersaturated solid solution HESA before aging. Thus, solutionized and water-quenched (SHT + WQ) samples had a meaningful microhardness enhancement after aging. By increasing the aging temperature from 800 °C to 900 °C, the microhardness value increased from 350.5 HV_1 (aged at 800 °C) to 395.4 HV_1 (aged at 900 °C). Further, increasing the aging temperature to 1000 °C did not enhance the microhardness value, suggesting potential over-aging started. Considering the size of γ' precipitate after SHT + WQ followed by aging treatment at 1000 °C (see Fig. 10B), it was obvious that γ' coarsening has occurred, which could be inappropriate for mechanical properties. Hence, based on the microhardness values and microstructural observations, solutionizing at 1190 °C followed by water-quenching and aging at 900 °C (water quenching) is recommended for the developed CoNi-based HESA via the SPS process.

Tensile properties – The room temperature tensile results of Sample C (SHT + WQ and aged at 900 °C) are depicted in Fig. 12B. The inclusion of two curves representing measurements from the same sample was employed to improve the precision of the tensile property evaluation. The obtained values for yield strength, ultimate tensile strength (UTS), and elongation were determined to be 612.5 ± 37.5 MPa, 760 ± 25.26 MPa, and 9.68 ± 0.28 %, respectively. Comparing the room temperature tensile properties of the SPSed and heat-treated sample to other outstanding CoNi-based superalloys, as indicated in previous studies [58,59], it is evident that the sample exhibits moderate tensile properties. This moderate behavior can be attributed to the formation of oxides, nitrides, and carbides during the Argon gas atomization process and thermal-induced porosities (TIPs) during heat treatment. The presence of impurities negatively impacts the tensile properties of the alloy. Furthermore, the incomplete bonding between particles observed in the EBSD results, particularly the presence of prior particle boundaries (PPBs), contributes to the compromised tensile results. Despite achieving a relative density of 99.9 % after the SPS process, the PPBs hinder complete bonding between the particles, thereby affecting the overall tensile strength and performance of the material. Similar findings have been reported by Sergi et al. [60] in their investigation of atomized IN 625 powder processed through hot isostatic pressing (HIP). They also observed incomplete bonding between particles, which had a detrimental effect on the mechanical properties of the alloy. Thus, it is crucial to conduct both powder production and sintering processes in a high-purity atmosphere to avoid the formation of oxides and nitrides, which can compromise the integrity and strength of the resulting material. According to the findings of Appa Rao et al. [61], the densification of consolidated IN718 through the HIP process is not influenced by the oxygen content. However, their research revealed that the formation of detrimental phases, such as PPBs, occurs more prominently in the HIPed material when using powder with high oxygen content.

Fractography – In PM samples, fractography analysis is particularly valuable for monitoring the influence of segregated elements and detrimental secondary phases. For this study, Fig. 13 illustrates the use

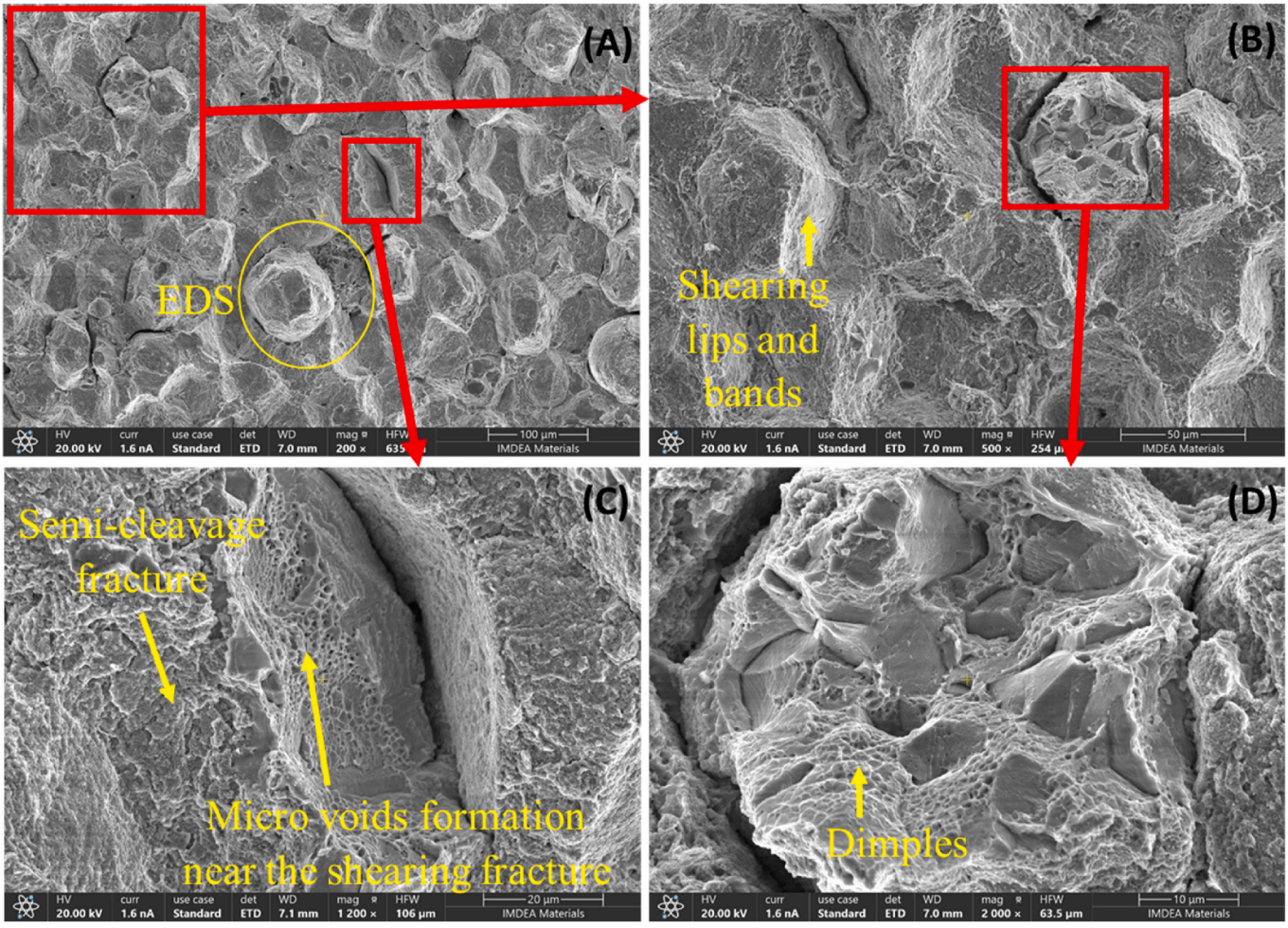


Fig. 13. Fractographic analysis of the fracture surface from the tensile test (Sample C, SHT + WQ and aged at 900 °C followed by water quenching).

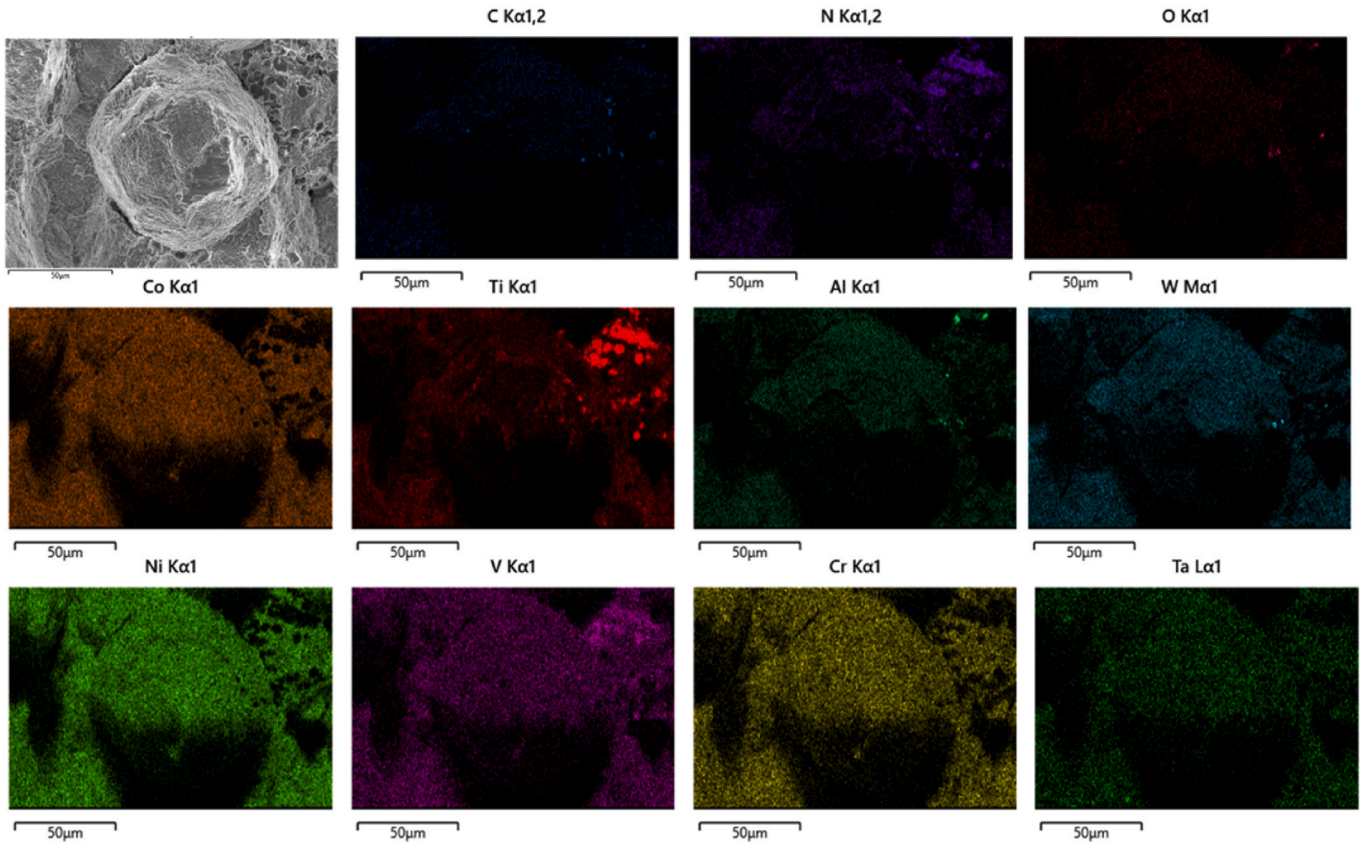


Fig. 14. EDS maps illustrate the elemental distribution on the fracture surface of the tensile sample, specifically corresponding to the region highlighted by the yellow circle in Fig. 13A. (For interpretation of the references to color in this figure legend, the reader is referred to the Web version of this article.)

of SEM to examine the fracture surface of the tensile test samples at both macro (lower magnification) and micro (higher magnification) scales. Upon analyzing the collected fractography images, no evidence of segregated elements or TCP phases was found. The primary fracture mechanism observed at the macro level indicates an inter-particle fracture, suggesting a brittle fracture occurring between the particles (Fig. 13A).

However, there are indications of certain micro-mechanisms at the particle interface, also known as the bonding zone, which involves a semi-cleavage pattern (see Fig. 13C). Additionally, the formation of ductile micro-voids is observed, likely resulting from micro-plastic deformation occurring prior to sample yielding and fracture. Moreover, the presence of ductile dimples on the surface of the fractured particle suggests a transgranular fracture mechanism (Fig. 13 D), indicating a semi-ductile to brittle fracture behavior. These findings highlight a complex fracture mechanism with both ductile and brittle characteristics operating at the microstructural level.

To further investigate the composition, EDS analysis was performed on a particle (highlighted by a yellow circle in Fig. 13A), and the results are presented in Fig. 14. The elemental distribution maps reveal a higher concentration of Ti- and V-rich nitrides without evidence of TCP phases or segregated intermetallics during manufacturing. Additionally, the EDS results indicate the presence of oxides and carbides. Overall, it is evident that the presence of PPBs has a significant influence on the tensile properties of the sample. The observation of inter-particle fracture, along with the impact of PPBs collectively contribute to the mechanical behavior of the material.

4. Conclusions

A novel high entropy superalloy design strategy was introduced based on CALPHAD calculations and HEAs principles. In this study, an octonary and single phase (FCC) CoNi-based HESA powder with $\Delta S_{mix} = 1.602R$ is successfully developed and consolidated using the SPS process. The SPS process parameters, including temperature, dwell time, and heating rate were optimized. Based on the CALPHAD calculations (TCNI11 database in ThermoCalc software), density measurements, mechanical properties, and microstructural observations, the optimum SPS condition was obtained at 1175 °C for a dwell time of 10 min and a heating rate of 100 °C.min^{-1}. Several heat treatment cycles were designed to achieve optimum post heat treatment cycles. The criteria of heat treatment pathway optimization were based on mean grain size, distribution and size of γ' precipitates, and Vickers microhardness values. Solutionizing at 1190 ± 10 °C for 2 h followed by water quenching resulted in grain size values of 6.9 ± 5.1 μm, similar to the measured mean grain size values of the SPS processed sample attained under the optimum condition. Further post heat treatment consisting of aging at 900 °C for 24 h followed by water quenching led to the formation of uniformly distributed fine γ' precipitates in the γ matrix without forming unwanted secondary precipitates and TCP phases in the matrix and grain boundaries. The results of this research have the potential to revolutionize the advanced manufacturing of CoNi-based HESAs for use in high-temperature environments.

CRediT authorship contribution statement

Ahad Mohammadzdeh: Conceptualization, Data curation, Funding acquisition, Investigation, Methodology, Resources, Software, Supervision, Writing – original draft. **Alessandro De Nardi:** Data curation, Formal analysis, Investigation. **Faraz Omidbakhsh:** Conceptualization, Formal analysis, Methodology, Writing – review & editing. **Dariusz Garbiec:** Investigation, Methodology, Writing – review & editing. **Ahmed Fardan:** Formal analysis, Software, Writing – review & editing. **Eduard Hryha:** Investigation, Methodology, Resources, Software,

Supervision, Writing – review & editing. **Amir Mostafaei:** Formal analysis, Investigation, Methodology, Writing – review & editing. **Jose Manuel Torralba:** Conceptualization, Data curation, Funding acquisition, Methodology, Project administration, Resources, Supervision, Writing – review & editing.

Declaration of competing interest

The authors declare that they have no known competing financial interests or personal relationships that could have appeared to influence the work reported in this paper.

Data availability

Data will be made available on request.

Acknowledgment

This investigation was supported by the European Union Horizon 2020 research and innovation program (Marie Sklodowska-Curie Individual Fellowships, Grant Agreement 101028155). A. Mostafaei would like to acknowledge the startup funding from the Department of Mechanical, Materials and Aerospace Engineering and Armour College of Engineering at Illinois Institute of Technology at Chicago, Illinois. Support within the framework of the Centre for Additive Manufacturing – Metal (CAM2), supported by the Swedish Governmental Agency of Innovation Systems (Vinnova), is acknowledged. A. De Nardi would like to acknowledge the grant "Research Initiation Fellowship 2023" (Excelencia María de Maeztu).

References

[1] J. Sato, T. Omori, K. Oikawa, I. Ohnuma, R. Kainuma, K. Ishida, Cobalt-base high-temperature alloys, Science 312 (2006) 90–91.
[2] A. Mostafaei, R. Ghiaasiaan, I.-T. Ho, S. Strayer, K.-C. Chang, N. Shamsaei, S. Shao, S. Paul, A.-C. Yeh, S. Tin, A.C. To, Additive Manufacturing of Nickel-based superalloys: a state-of-the-art review on process-structure-defect-property relationship, Prog. Mater. Sci. 136 (2023) 101108, https://doi.org/10.1016/j.pmatsci.2023.101108.
[3] S.K. Makineni, B. Nithin, K. Chattopadhyay, Synthesis of a new tungsten-free γ–γ′ cobalt-based superalloy by tuning alloying additions, Acta Mater. 85 (2015) 85–94, https://doi.org/10.1016/j.actamat.2014.11.016.
[4] W.-W. Xu, Overview γ'-strengthened of the development cobalt-base superalloys of L12, Adv. Multicomponent Alloy. From Fundam. to Appl. (2022) 155.
[5] M. Cartón-Cordero, M. Campos, L.P. Freund, M. Kolb, S. Neumeier, M. Göken, J. M. Torralba, Microstructure and compression strength of Co-based superalloys hardened by γ′ and carbide precipitation, Mater. Sci. Eng. 734 (2018) 437–444, https://doi.org/10.1016/j.msea.2018.08.007.
[6] M. Cartón-Cordero, B. Srinivasarao, M. Campos, A. García-Junceda, J.M. Torralba, On the role of processing parameters in sintered new Co-based (W,Al) alloys, J. Alloys Compd. 674 (2016) 406–412, https://doi.org/10.1016/j.jallcom.2016.03.077.
[7] F. Xue, H.J. Zhou, X.F. Ding, M.L. Wang, Q. Feng, Improved high temperature γ′ stability of Co–Al–W-base alloys containing Ti and Ta, Mater, Letture 112 (2013) 215–218, https://doi.org/10.1016/j.matlet.2013.09.023.
[8] P. Pandey, N. Mazumder, M.P. Singh, C. Patil, A. Sharma, S.K. Makineni, D. Banerjee, K. Chattopadhyay, Design of low mass density γ/γ' CoNi-based superalloys with promising high-temperature mechanical properties, Phys. Rev. Mater. 5 (2021) 93601, https://doi.org/10.1103/PhysRevMaterials.5.093601.
[9] C. Chu, Q. Guo, R. Ding, Y. Liu, The effects of Ti and Ta on the microstructure and high temperature deformation mechanisms of the CoNi-based superalloys, Mater. Char. 199 (2023) 112841, https://doi.org/10.1016/j.matchar.2023.112841.
[10] T. Omori, K. Oikawa, J. Sato, I. Ohnuma, U.R. Kattner, R. Kainuma, K. Ishida, Partition behavior of alloying elements and phase transformation temperatures in Co–Al–W-base quaternary systems, Intermetallics 32 (2013) 274–283, https://doi.org/10.1016/j.intermet.2012.07.033.
[11] H.-Y. Yan, V.A. Vorontsov, D. Dye, Alloying effects in polycrystalline γ′ strengthened Co–Al–W base alloys, Intermetallics 48 (2014) 44–53, https://doi.org/10.1016/j.intermet.2013.10.022.
[12] A. Bauer, S. Neumeier, F. Pyczak, M. Göken, Microstructure and creep strength of different γ/γ′-strengthened Co-base superalloy variants, Scripta Mater. 63 (2010) 1197–1200, https://doi.org/10.1016/j.scriptamat.2010.08.036.
[13] S. Kobayashi, Y. Tsukamoto, T. Takasugi, The effects of alloying elements (Ta, Hf) on the thermodynamic stability of γ′-Co3(Al,W) phase, Intermetallics 31 (2012) 94–98, https://doi.org/10.1016/j.intermet.2012.06.006.
[14] Effects of Ni, Cr and W on the Microstructural Stability of Multicomponent CoNi-Base Superalloys Studied Using CALPHAD and Diffusion-Multiple Approaches | Elsevier Enhanced Reader, (n.d.).
[15] K. Shinagawa, T. Omori, J. Sato, K. Oikawa, I. Ohnuma, R. Kainuma, K. Ishida, Phase equilibria and microstructure on γ′ phase in Co-Ni-Al-W system, Mater. Trans. 49 (2008) 1474–1479.
[16] W. Li, L. Li, S. Antonov, Q. Feng, Effective design of a Co-Ni-Al-W-Ta-Ti alloy with high γ′ solvus temperature and microstructural stability using combined CALPHAD and experimental approaches, Mater. Des. 180 (2019) 107912, https://doi.org/10.1016/j.matdes.2019.107912.
[17] D.S. Ng, D.-W. Chung, J.P. Toinin, D.N. Seidman, D.C. Dunand, E.A. Lass, Effect of Cr additions on a γ-γ' microstructure and creep behavior of a Co-based superalloy with low W content, Mater. Sci. Eng. 778 (2020) 139108, https://doi.org/10.1016/j.msea.2020.139108.
[18] N. Volz, C.H. Zenk, R. Cherukuri, T. Kalfhaus, M. Weiser, S.K. Makineni, C. Betzing, M. Lenz, B. Gault, S.G. Fries, J. Schreuer, R. Vaßen, S. Virtanen, D. Raabe, E. Spiecker, S. Neumeier, M. Göken, Thermophysical and mechanical properties of advanced single crystalline Co-base superalloys, Met. Mater. Trans. (2018) 1–11. https://www.scopus.com/inward/record.uri?eid=2-s2.0-85060241575&partnerID=40&md5=c34a92f1eb956f38ac177f290293ce5b.
[19] B.X. Cao, H.J. Kong, Z.Y. Ding, S.W. Wu, J.H. Luan, Z.B. Jiao, J. Lu, C.T. Liu, T. Yang, A novel L12-strengthened multicomponent Co-rich high-entropy alloy with both high γ′-solvus temperature and superior high-temperature strength, Scripta Mater. 199 (2021) 113826.
[20] E.A. Lass, Application of computational thermodynamics to the design of a Co-Ni-based γ′-strengthened superalloy, Metall. Mater. Trans. A Phys. Metall. Mater. Sci. 48 (2017) 2443–2459, https://doi.org/10.1007/s11661-017-4040-y.
[21] E.A. Lass, D.J. Sauza, D.C. Dunand, D.N. Seidman, Multicomponent γ'-strengthened Co-based superalloys with increased solvus temperatures and reduced mass densities, Acta Mater. 147 (2018) 284–295, https://doi.org/10.1016/j.actamat.2018.01.034.
[22] X. Zhuang, S. Antonov, W. Li, S. Lu, L. Li, Q. Feng, Alloying effects and effective alloy design of high-Cr CoNi-based superalloys via a high-throughput experiments and machine learning framework, Acta Mater. 243 (2023) 118525, https://doi.org/10.1016/j.actamat.2022.118525.
[23] X. Zhuang, S. Lu, L. Li, Q. Feng, Microstructures and properties of a novel γ′-strengthened multi-component CoNi-based wrought superalloy designed by CALPHAD method, Mater. Sci. Eng. 780 (2020) 139219, https://doi.org/10.1016/j.msea.2020.139219.
[24] J.-W. Yeh, S.-J. Lin, Breakthrough applications of high-entropy materials, J. Mater. Res. 33 (2018) 3129–3137.
[25] Y.E.H. Jien-Wei, Recent progress in high entropy alloys, Ann. Chim. Sci. Mat. 31 (2006) 633–648.
[26] R. Feng, P.K. Liaw, M.C. Gao, M. Widom, First-principles prediction of high-entropy-alloy stability, npj Comput. Mater. 3 (2017) 50, https://doi.org/10.1038/s41524-017-0049-4.
[27] F. Li, Y. Sha, X. Zeng, S. Zhang, T. Shi, B. Shen, Q. Shen, M. Liu, A new criterion for prediction of phase stability in Al-containing high entropy alloys, Phys. Status Solidi 258 (2021) 2000470.
[28] A. Mohammadzadeh, A. Heidarzadeh, H. Becker, J.V. Robles, A. Meza, M. Avella, M.A. Monclús, D. Tourret, J.M. Torralba, Exploring the impact of configurational entropy on the design and development of CoNi-based superalloys for sustainable applications, J. Alloys Compd. (2023) 171380, https://doi.org/10.1016/j.jallcom.2023.171380.
[29] R. Jain, M.R. Rahul, P. Chakraborty, R.K. Sabat, S. Samal, G. Phanikumar, R. Tewari, Design and deformation characteristics of single-phase Co-Cr-Fe-Ni-V high entropy alloy, J. Alloys Compd. 888 (2021) 161579, https://doi.org/10.1016/j.jallcom.2021.161579.
[30] M.C. Gao, R. Arróyave, J.E. Morral, U.R. Kattner, Thermodynamics and kinetics of high-entropy alloys, J. Phase Equilibria Diffus. 42 (2021) 549–550, https://doi.org/10.1007/s11669-021-00923-8.
[31] P. Chakraborty, A. Sarkar, K. Ali, J. Jha, N. Jothilakshmi, A. Arya, R. Tewari, Design and development of low density, high strength ZrNbAlVTi high entropy alloy for high temperature applications, Int. J. Refract. Met. Hard Mater. 113 (2023) 106222, https://doi.org/10.1016/j.ijrmhm.2023.106222.
[32] T. Froeliger, A. Després, L. Toualbi, D. Locq, M. Veron, G. Martin, R. Dendievel, Interplay between solidification microsegregation and complex precipitation in a γ/γ' cobalt-based superalloy elaborated by directed energy deposition, Mater. Char. 194 (2022) 112376, https://doi.org/10.1016/j.matchar.2022.112376.
[33] R. Casas, F. Galvez, M. Campos, Microstructure stability and hardening determination through heat treatment of sintered Co γ/γ′ based alloys, Powder Metall. 65 (2022) 242–252, https://doi.org/10.1080/00325899.2021.1994116.
[34] R. Casas, R. Sancho, M. Campos, F. Gálvez, The effect of temperature on the high-strain-rate response of Co-Al-W- base alloys: experiments and modeling, J. Alloys Compd. 897 (2022) 163154, https://doi.org/10.1016/j.jallcom.2021.163154.
[35] L. Zhang, X.B. He, X.H. Qu, R.U. Din, H.S. Liu, D. Li, H.M. Zhu, Microstructural Formation in novel Co-base ODS alloys produced by mechanical alloying, Adv. Mater. Res. 415–417 (2012) 1136–1139. https://doi.org/10.4028/www.scientific.net/AMR.415-417.1136.
[36] L. Zhang, X. Qu, X. He, R. Din, H. Liu, M. Qin, H. Zhu, Microstructural characterization of Co-based ODS alloys, J. Mater. Eng. Perform. 21 (2012) 2487–2494, https://doi.org/10.1007/s11665-012-0206-3.
[37] L. Zhang, X. Qu, X. He, D. Rafi-ud, M. Qin, H. Zhu, Hot deformation behavior of Co-base ODS alloys, J. Alloys Compd. 512 (2012) 39–46, https://doi.org/10.1016/j.jallcom.2011.08.097.

[38] M. Knop, P. Mulvey, F. Ismail, A. Radecka, K.M. Rahman, T.C. Lindley, B. A. Shollock, M.C. Hardy, M.P. Moody, T.L. Martin, A new polycrystalline Co-Ni superalloy, Jom 66 (2014) 2495–2501.
[39] M. Khoshghadam-Pireyousefan, A. Mohammadzadeh, A. Heidarzadeh, D. Brabazon, Fundamentals of Spark Plasma Sintering for Metallic, Ceramic, and Polymer Matrix Composites Production, 2021.
[40] A. Mohammadzadeh, M. Azadbeh, H. Danninger, A.S. Namini, Ti–TiB_2 composites consolidated by spark plasma sintering: reaction mechanism, characteristics of in-situ formed phases and densification behavior, Mater. Chem. Phys. 242 (2020), https://doi.org/10.1016/j.matchemphys.2019.122556.
[41] A. Mohammadzadeh, A. Sabahi Namini, M. Azadbeh, A. Motallebzadeh, On the physical and mechanical properties of spark plasma sintered pure Ti and Ti-TiB composite, Mater. Res. Express 5 (2018) 126512, https://doi.org/10.1088/2053-1591/aae057.
[42] M. Fattahi, A. Mohammadzadeh, Y. Pazhouhanfar, S. Shaddel, M. Shahedi Asl, A. Sabahi Namini, Influence of SPS temperature on the properties of TiC–SiC_w composites, Ceram. Int. 46 (2020), https://doi.org/10.1016/j.ceramint.2020.01.206.
[43] X.I.E. Leipeng, C. Minghui, W. Jinlong, W. Fuhui, High temperature oxidation behavior of ultrafine grained ODS nickel-based superalloy prepared by spark plasma sintering, J. Chin. Soc. Corrosion Protect 42 (2022) 709–716.
[44] L. Yu, Z. Lu, S. Peng, X. Li, Effect of Al/Ti ratio on γ′ and oxide dispersion strengthening in Ni-based ODS superalloys, Mater. Sci. Eng. 845 (2022) 143240.
[45] S. Yan, W. Zhai, J. Xiao, W. Zhai, A.M.M. Ibrahim, Graphene oxide decorated spherical powder for Ni superalloy with high yield strength and ductility, Mater. Sci. Eng. 831 (2022) 142221.
[46] C.A.C.A. Schneider, W.S.W.S. Rasband, K.W.K.W. Eliceiri, NIH Image to ImageJ: 25 years of image analysis, Nat. Methods 9 (2012) 671–675, https://doi.org/10.1038/nmeth.2089.
[47] A. Standard, E8. Standard Test Method for Tension Testing of Metallic Materials, ASTM, West Conshohocken, 2004.
[48] Z. Liang, S. Neumeier, Z. Rao, M. Göken, F. Pyczak, CALPHAD informed design of multicomponent CoNiCr-based superalloys exhibiting large lattice misfit and high yield stress, Mater. Sci. Eng. 854 (2022) 143798, https://doi.org/10.1016/j.msea.2022.143798.
[49] O.N. Senkov, S. V Senkova, C. Woodward, Effect of aluminum on the microstructure and properties of two refractory high-entropy alloys, Acta Mater. 68 (2014) 214–228, https://doi.org/10.1016/j.actamat.2014.01.029.
[50] X. Yang, Y. Zhang, Prediction of high-entropy stabilized solid-solution in multi-component alloys, Mater. Chem. Phys. 132 (2012) 233–238.
[51] F. Xue, M. Wang, Q. Feng, Alloying effects on heat-treated microstructure in Co-Al-W-base superalloys at 1300 C and 900 C, Superalloys 2012 (2012) 813–821.
[52] L. Wang, M. Oehring, Y. Li, L. Song, Y. Liu, A. Stark, U. Lorenz, F. Pyczak, Microstructure, phase stability and element partitioning of γ-γ′ Co-9Al-9W-2X alloys in different annealing conditions, J. Alloys Compd. 787 (2019) 594–605.
[53] M. Wen, Y. Sun, J. Yu, Y. Yang, Y. Zhou, X. Sun, Effects of Al content on microstructures and high-temperature tensile properties of two newly designed CoNi-base superalloys, J. Alloys Compd. 835 (2020) 155337.
[54] A. Mehta, Y. Sohn, High entropy and sluggish diffusion “core” effects in senary FCC Al–Co–Cr–Fe–Ni–Mn alloys, ACS Comb. Sci. 22 (2020) 757–767, https://doi.org/10.1021/acscombsci.0c00096.
[55] K.-Y. Tsai, M.-H. Tsai, J.-W. Yeh, Sluggish diffusion in Co–Cr–Fe–Mn–Ni high-entropy alloys, Acta Mater. 61 (2013) 4887–4897, https://doi.org/10.1016/j.actamat.2013.04.058.
[56] T. Koyama, Y. Tsukada, T. Abe, Simple approach for evaluating the possibility of sluggish diffusion in high-entropy alloys, J. Phase Equilibria Diffus. 43 (2022) 68–77, https://doi.org/10.1007/s11669-022-00938-9.
[57] P.J. Bocchini, C.K. Sudbrack, R.D. Noebe, D.C. Dunand, D.N. Seidman, Effects of titanium substitutions for aluminum and tungsten in Co-10Ni-9Al-9W (at%) superalloys, Mater. Sci. Eng. 705 (2017) 122–132.
[58] P. Pandey, M. Heczko, N. Khatavkar, N. Mazumder, A. Sharma, A. Singh, M. J. Mills, K. Chattopadhyay, On the faulting and twinning mediated strengthening and plasticity in a γ' strengthened CoNi-based superalloy at room temperature, Acta Mater. 252 (2023) 118928, https://doi.org/10.1016/j.actamat.2023.118928.
[59] S.P. Murray, K.M. Pusch, A.T. Polonsky, C.J. Torbet, G.G.E. Seward, P. Nandwana, M.M. Kirka, R.R. Dehoff, N. Zhou, S.A.J. Forsik, W. Slye, T.M. Pollock, in: S. Tin, M. Hardy, J. Clews, J. Cormier, Q. Feng, J. Marcin, C. O’Brien, A. Suzuki (Eds.), Microstructure and Tensile Properties of a CoNi-Based Superalloy Fabricated by Selective Electron Beam Melting BT - Superalloys 2020, Springer International Publishing, Cham, 2020, pp. 880–890.
[60] A. Sergi, R.H.U. Khan, M.M. Attallah, The role of powder atomisation route on the microstructure and mechanical properties of hot isostatically pressed Inconel 625, Mater. Sci. Eng. 808 (2021) 140950, https://doi.org/10.1016/j.msea.2021.140950.
[61] G.A. Rao, M. Srinivas, D.S. Sarma, Effect of oxygen content of powder on microstructure and mechanical properties of hot isostatically pressed superalloy Inconel 718, Mater. Sci. Eng. 435–436 (2006) 84–99, https://doi.org/10.1016/j.msea.2006.07.053.